2008

CELLULAR MRI: TRACKING THE MIGRATION OF METASTATIC CANCER CELLS IN THE LYMPHATIC SYSTEM

Tracey Y.M. Lui
Western University

CELLULAR MRI: TRACKING THE MIGRATION OF

METASTATIC CANCER CELLS IN THE LYMPHATIC SYSTEM

(Spine Title: Cellular MRI: Tracking Metastatic Cancer in the Lymphatic System)
(Thesis Format: Integrated Article)

by

Tracey Y.M. Lui

Graduate Program
in
Medical Biophysics

Submitted in partial fulfillment
of the requirements for the degree of
Master of Science

School of Graduate and Postdoctoral Studies
The University of Western Ontario
London, Ontario
August 2008

Abstract

The role of the lymphatics as a mode of tumor cell transport has been known for some time, and remains of critical importance since a majority of cancer deaths result from metastatic dissemination away from the primary tumor. In the studies performed in this thesis novel cellular MRI technology and a unique murine intranodal implantation model are used to track the movement of iron-labeled melanoma cells in vivo. With these methods we demonstrate, for the first time, that cellular MRI can be used to detect metastatic melanoma cells present at the implant site and in the draining lymph node and to track the growth of these cells into a metastatic tumor. The ability to track metastatic cancer cells in the lymphatic system in vivo may promote a better understanding of models of carcinogenesis and metastasis and in the future may help to improve on principles by which cancers are treated.

Keywords: Magnetic Resonance Imaging (MRI); balanced steady-state free precession (b-SSFP); superparamagnetic iron-oxide particles (SPIO); melanoma; B16F10; lymphatic metastasis; mouse model.

TABLE OF CONTENTS

List of Figures

List of Tables

List of Equations

List of Acronyms and Abbreviations

AMNP	Anionic Iron-Oxide
b-SSFP	Balanced-Steady State Free Precession
CCL21/19	Chemokine (C-C motif) ligand 21/19
CCR7	Chemokine (C-C motif) receptor 7
CLIO	Cross-linked Iron-oxide
CT	Computed Tomography
DMBA	7,12-dimethylbanz(a)anthracene
DMEM	Dulbecco's modified Eagle's medium
EAE	Autoimmune encephalomyelitis
FBS	Fetal Bovine Serum
FDG	2-18F-fluoro-2-deoxy-D-glucose
FID	Free Induction Decay
Gad	Gadolinium
Gd-BOPTA	Gadobenate dimeglumine
Gd-DTPA	Gadopentetate dimeglumine
GRE	Gradient Echo
H&E	Hematoxylin and eosin
HBSS	Hank's Balanced Salt Solution
ICP-MS	Inductively Couple Mass Spectrometry
IV	Intravenous
IVVM	Intravital videomicroscopy
MION	Monocystalline
MNP	Magnetic Nanoparticles
MPF	Mammary Fat Pad
MPIO	Micron-sized Superparamagnetic Iron-Oxide
MRI	Magnetic Resonance Imaging
MS	Multiple Sclerosis
MHz	Megahertz
NMR	Nuclear Magnetic Resonance
PBS	Phosphate Buffered Saline
PET	Positron Emission Tomography
PLL	Poly-L-lysine
PPB	Perl's Prussian Blue
PTHrP	Parathyroid hormone-related peptide
RF	Radiofrequency
SE	Spin Echo
SLN	Sentinel Lymph Node
SNR	Signal-to-Noise Ratio
SPIO	Superparamagnetic Iron-Oxide
SSFP	Steady State Free Precession
T	Telsa
TE	Echo Time
TR	Repetition Time
US	Ultrasound

USPIO	Ultrasmall Superparamagnetic Iron-Oxide
VEGFC	Vascular Endothelial Growth Factor-C
VEGFD	Vascular Endothelial Growth Factor-D
VEGFR2	Vascular Endothelial Growth Receptor 2
VEGFR3	Vascular Endothelial Growth Receptor 3

List of Symbols

s	Spin
$\bar{S}$	Spin angular momentum
$\bar{\mu}$	Magnetic dipole moment
γ	Gyromagnetic ratio
T	Telsa
M	Magnetization
M_o	Net magnetization
M_{xy}	Magnetization in the transverse plane
M_z	Magnetization on the z-axis
ω_o	Larmour Frequency
B_ϕ	Main Magnetic Field
B_1	Oscillating magnetic field
α	Flip Angle

List of Appendices

Chapter 1 : Introduction

1.1   Metastasis

Metastasis is the spread of malignant cells from the original tumor (1). This spreading of cancer cells causes 90% of deaths related to solid tumors (2). The steps of metastasis are correlated and are all considered crucial to the development of metastatic growths. In order for a primary tumor to continue to proliferate it must develop its own blood vessels, a process known as angiogenesis. Cells can then escape from the primary tumor and enter distant tissues directly through circulatory system or indirectly through the lymphatic system (3). In the circulatory system, they must be able to survive transport. Size restrictions of the capillaries will limit further migration of the cells and the cells can extravasate out of the blood vessels and into the new tissue. If the cells can survive after arrest in the secondary organ they can exist in the tissue as solitary cells, small pre-angiogenic or large vascularized metastases (4). Solitary cells or dormant cells are cells that are thought to be quiescent and are neither proliferating nor undergoing apoptosis (5). These cells have been thought to have a role in cancer reoccurrence that appears after seemingly successful treatment and can even occur several years post therapy. Dormant cancer cells are believed to be immune to chemotherapy since most chemotherapy drugs are directed at cells that are rapidly dividing (6). Fortunately, metastasis is an inefficient process since very few cells that are released from the primary tumor actually develop into secondary tumors (7).

The survival of cancer cells at the secondary site is dependent upon where the cells arrest after extravasation. In 1889, Dr. Stephen Paget proposed the "seed" and "soil" theory; the

"seed" is the cancer cell and the "soil" is the tissue in which it can grow. Paget hypothesized that the development of metastases at a distant site was not a chance event but that the tissue was predisposed to certain types of secondary tumors (8). Since then the propensity for metastatic tumors to develop in specific organs has been demonstrated (9-11). An opposing theory for metastasis is that cancer cells are not predisposed to develop in certain tissues and that the site of metastasis is only dependent on mechanical factors, such as the location of the primary tumor and circulatory patterns. Studies have also emerged to support this theory (12-14). However, it is now accepted that metastasis is likely a mixture of both these theories and that one is not exclusive from the other (4).

1.1.1 Metastasis in the Lymphatic System

The role of the lymphatic system in the body is threefold. It transports the fat-soluble material, such as triglycerides and fat-soluble vitamins, from the digestive tract, it drains the excess fluid from the interstitial spaces of the body and returns it to the body via the circulatory system and it provides immune responses and resistance to disease such as cancer (15, 16). The importance of the lymphatic system in metastasis has been known for over 200 years (17) and the lymph nodes are a common site of metastasis for various cancers (16, 18). Only recently have possible mechanisms of metastatic spread to the lymphatics been described (19, 20). The previous focus on metastasis has largely been on the circulatory system and angiogenesis. There is still a need to characterize metastatic processes like intravasation, survival, and extravasation in the lymphatic system.

Metastatic cancer cells can enter the lymphatic system as part of the lymph fluid. As a primary tumor becomes larger the intratumoral fluid pressure increases and fluid leaks into

the interstitial space increasing its pressure. In light of this buildup, the lymphatic capillaries will increase in diameter and open intercellular junctions. The lymph and cells that have disseminated from the primary tumor now have easy entry into the lymphatic vessels. Once cells have entered the lymphatic vessels they can adhere to the vessel wall and extravasate into the surrounding tissue. They can also enter the subcapular sinus of the regional lymph node(s) via the afferent lymphatic vessel and invade the cortex of the node or leave the node through the efferent lymphatic vessel to travel to other nodes, or drain into the circulatory system (17). Lymph nodes have been shown to be useful as a mechanical barrier against cancer cells but ultimately fail as a biological barrier against metastasis (21). Recently it has been shown that metastatic cells may have a more active role in finding their way into the lymphatic system. CCL21/19 are ligands that secreted by the lymphatics to help dendritic and memory T cells migrate to the lymphatic system. Cancer cells have been shown to secrete CCR7 a ligand for CCL21/19. These molecules then drain to the closest working lymphatic vessel forming a chemotatic gradient. Cancer cells can then follow this gradient and "home" to the lymphatic system (22).

Lymphangiogenesis is also being purposed as a means for cancer cells to migrate via the lymphatics (16, 17). Analogous to angiogenesis, lymphangiogenesis is the formation of new lymphatic vessels (23). Vascular endothelial growth factors-C and D (VEGFC and VEGFD) binds to the VEGFR2 and VEGFR3 found on the surface of lymphatic vessels. This promotes the proliferation of new lymphatic vessels and influence metastatic development in the lymphatic system (1). The exact relationship between lymphangiogenesis and metastasis still needs to be determined but this process has the potential to be a target for

therapeutics, as lymphatic vessels within the tumor could provide another means of escape for disseminated cancer cells.

1.1.2   Metastatic Melanoma

Melanoma is the result of mutations in the melanocytes of the skin. It is the rarest form of skin cancer but it is also the most dangerous (24). During 2007, there were 4,600 new cases of melanoma in Canada and it was one of only three types of cancer to show an increase of >2% in new incidences between 1994-2003 (25). Multiple risk factors, both genetic and environmental, are associated with the development of the disease. People with mutations in the CDKN2A (or p16), a tumor suppressor gene, and the CDK4 gene have a predisposition to melanoma (26). Phenotypic characteristics such as fair skin, red hair, freckles, and inability to tan have also been linked with melanoma. Exposure to sunlight, especially during childhood, has been found to be the primary environmental cause of melanoma. An estimated 65% of the world's melanoma cases are a direct result of sunlight (27).

Prognostic factors for melanoma include the patient's age and sex, tumor location, ulceration, tumor thickness and lymph node status. Survival rates have been shown to decrease with age and females tend to survive longer than men (28). It has been shown that patients with a tumor growth ≤ 1 mm without ulceration have a 95% five-year survival rate while a growth of > 4.0 mm with an ulceration shows a five-year survival rate of 45% (28). Lymph node involvement is the most important prognostic factor for patient survival (29). The development of sentinel lymph node (SLN) biopsy has been shown to be a more effective prognostic technique than elective lymph node dissection and carries less risk of

morbidity and complications (24). The SLN, which is the first draining node of the tumor, is identified for removal using a radioactive and/or dye tracers (29). Disease in the SLN has been shown to be representative of the disease status of the entire nodal basin; a larger number of SLN with disease and a larger tumor burden within the SLN corresponds to a decrease in patient survival rates (28). However the clinical significance of micrometastasis within the SLN is controversial and the interpretation of this result is still unclear (30).

The mouse melanoma cell line B16F0 and its variants are widely used to study melanoma metastasis. The B16F0 cell line was cultured from a spontaneously occurring melanoma in a C57Bl/6J mouse in 1954 (31). In 1973 Fidler isolated two subclones with differences in metastatic ability from the original cell line: B16F1, which has low metastatic potential and is unlikely to metastasize to the visceral organs, and B16F10, which has high metastatic potential (32). These are the mostly commonly used B16 cell lines for murine experiments. Numerous other subclones have been isolated since then and include: B16-BL6 which aggressively metastasizes to the bladder, B1-O10 which preferentially metastasizes to the ovaries (33) and B16-B10b which preferentially metastasizes to the brain (34).

A variety of routes of administration of B16 cells have been investigated. The subcutaneous injection of B16 cells into the tail has been studied and results in adenopathy of the inguinal lymph nodes and metastasis to the lung. However, resection of the primary tumor by amputating the tail is necessary before 6 weeks post injection to avoid ulceration of the tumor (35). Subcutaneous footpad injections of B16F1, B16F10, and B16BL6 results in metastasis to the popliteal lymph node but also requires amputation of the leg 3 weeks post-injection (36). Subcutaneous injection of B16F1 on the flank results in metastasis to the para-

aortic/pelvic lymph nodes (37). These models are advantageous as they imitate the natural progression of cancer from the formation of the primary tumor followed by involvement of the regional lymph nodes and then metastasis to the organs. Other models of B16 metastasis include an intracardiac injection of cells resulting in a model of bone metastasis (38) and an intravenous injection for a model of lung metastasis (39). These models bypass the dissemination of cells from the primary tumor but are useful to study cell and secondary organ interactions. In this thesis I have used the direct intranodal implantation of B16F10 cells to track cancer cells in the lymphatics (40).

1.1.3 *Methods to Study Metastasis*

Histology was developed in the late 1800's, is extremely sensitive and can be used to study single cells. Histology involves tissue fixation, embedding, sectioning, mounting and staining (41). Stains are used to increase the contrast between cells and the organelles within them. When dyes are tagged to antibodies, individual cells of interest can be identified (42). This has been the method typically used to study metastasis. Histology offers a detailed look at the events in the metastatic process but can only provide a snap shot of one point in time. In-vivo imaging methods offer opportunities to study the dynamic processes involved in metastasis.

Optical imaging techniques, such as bioluminescence and fluorescence imaging and intravital videomicroscopy (IVVM), offer the highest image resolution with the ability to image single cells in-vivo in real time. Using IVVM and a cell counting technique, where inert beads are injected with cancer cells at a known ratio, it was found that the rate limiting steps in hematologic metastasis are the initiation of growth after the extravasation of

6

metastatic cancer cells followed by the ability of the micrometastases to develop angiogenesis to continued growth (7). New contrast agents using viral nanoparticles conjugated to fluorescent dyes can be taken up by endothelial cells and offer the opportunity visualize angiogenesis in-vivo using fluorescence imaging (43). However, optical techniques are limited by depth and require invasive procedures, which is undesirable for longitudinal imaging. Computed tomography (CT) offers high resolution scanning and fast scan times. Cellular imaging with CT has shown that macrophages, labeled with an iodine based contrast agent, can be imaged infiltrating atherosclerotic plaques. Histological results showed that the amount of macrophages within the plaque corresponded with strong enhancement seen in the CT images (44). Unfortunately CT utilizes ionizing radiation and lacks soft tissue contrast. Positron emission tomography (PET) detects cellular and molecular events using radiolabeled probes and is an extremely sensitive technique. $2\text{-}^{18}F\text{-}$fluoro-2-deoxy-D-glucose (FDG) is a tracer used in PET and is transported into the cell like regular glucose but cannot be used for glycolysis thus the cell can be detected. The internalization of the contrast agent is related to metabolic activity and cancer cells have high metabolisms. However, PET does not give any anatomical information and has poor resolution (45). High frequency ultrasound (US) is a fast and inexpensive method to produce high resolution images of approximately 50 μm in mice. Like optical techniques, high-frequency US is limited by depth. US has high soft tissue contrast but the field of view of US is also limited such that the organ or tissue of interest must be known before it can be scanned (46, 47).

MRI offers the opportunity for high resolution imaging, superior soft-tissue contrast, is depth independent, can image the entire mouse body and is sensitive enough to detect single

7

iron-labeled cells in-vivo (48, 49). Recently our lab has shown that as few as 100 B16F10 cells can be detected, in-vivo with MRI, within the mouse lymph node (40). The main downside to MRI is long scan times. But the benefits of MRI override its limitations and it is our lab's modality of choice to study disease. More studies are emerging that involve multi-modalities to capitalize on the advantages of each technique (50-52).

1.2   MR Imaging

1.2.1   Magnetism

Magnetism is a result of moving electric charges. Atoms with an odd number of protons and/or an odd number of neutrons have an intrinsic angular momentum or spin denoted by s (s=1/2 for protons), which results in spin angular momentum $\vec{S}$ and produces a small magnetic moment $\vec{\mu}$.
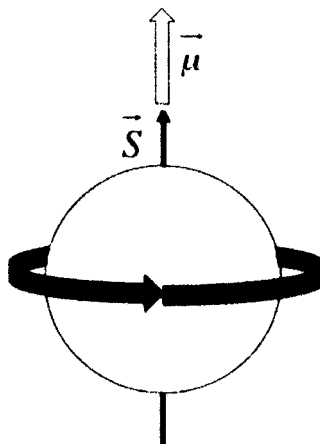
Figure 1.1: Proton Spin

The orientation of the magnetic moment is along the spin axis and its magnitude is given by:

$$\bar{\mu} = \gamma \bar{S}$$

Equation 1.1: Magnetic Moment

where γ is the gyromagnetic ratio and is specific for every atom. γ for hydrogen is 42.577 Mz/T (53).

The most abundant atom in the human body is hydrogen, which contains one proton and has its own magnetic moment. MR imaging usually consists of imaging protons and the remainder of this discussion on MRI will refer to them. Protons in a sample are randomly oriented and so are their magnetic moments. This random orientation results in the moments canceling each other out and as a result the net magnetic moment is zero (54). If that sample were to be placed within a strong external magnetic field $B_\emptyset$, then the magnetic moments should align with the field, either in the same direction as the magnetic field (parallel) or in the opposite direction of the magnetic field (antiparallel). By convention the direction of B_o is defined to be in the z-direction (along the long axis of the magnet).

The protons preferentially orient themselves in the parallel state since it is of lower energy. Thus the sum of all the magnetic moments, for a sample in a magnetic field, results in net magnetic moment, M_o that is in same direction as $B_\emptyset$. The actual orientation of the protons is slightly tipped away from the B_o axis (55).
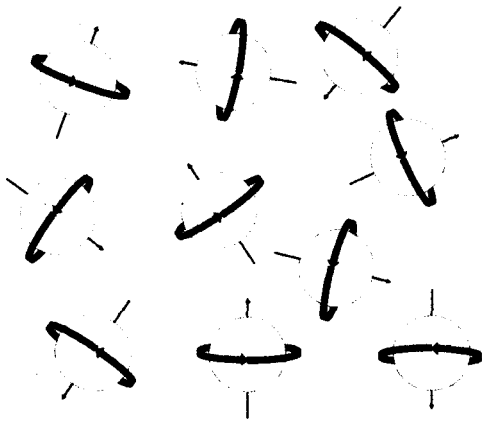
Figure 1.2: Proton in their Natural State   **Figure 1.3: Protons within Bø**
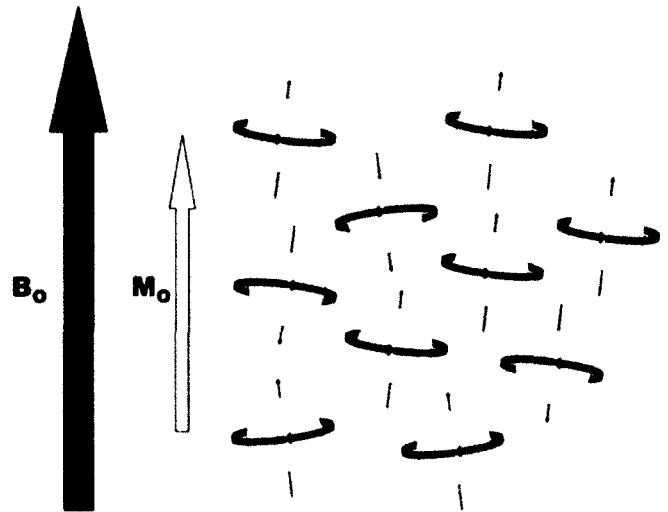
The proton experiences a torque once an external magnetic field is applied and precesses at a well-defined frequency. This frequency is determined by:

$$\omega_o = \gamma B_\phi$$

Equation 1.2: Larmour Frequency

This simple but incredibility important equation is known as the Larmour (or resonance) equation (55).

1.2.2   Nuclear Magnetic Resonance

When a radiofrequency (RF) pulse is applied to a sample within an external magnetic field, at a frequency that matches the resonance frequency of the proton within that sample, energy will be absorbed by the proton causing it to become excited and jump into the higher energy state. Described classically this induces a torque on M_o causing it to rotate away

from the z-axis (53). This is known as nuclear magnetic resonance (NMR). For an observer looking at this system from a stationary frame of reference (the laboratory frame of reference, with co-ordinates x, y, and z), M_o would seem to spiral down into the xy or transverse plane. If the observer were to view this system standing on the M_o vector, then in this rotating frame of reference (with co-ordinates x′, y′, and z′) M_o can be seen as tipping smoothly down into the transverse plane (55).
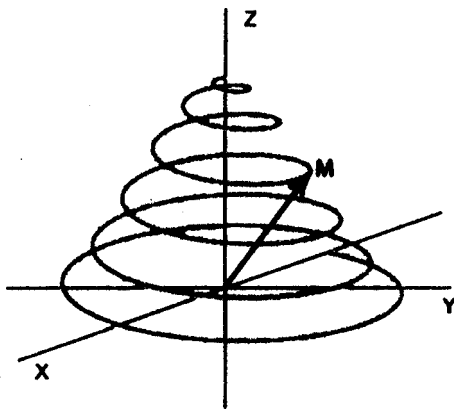
Figure 1.4: M_o in Lab Frame of Reference
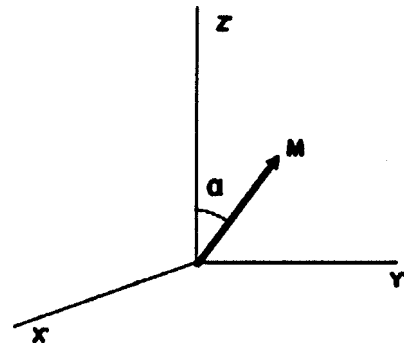
Figure 1.5: M_o in Rotating Frame of Reference

When a rectangular pulse is applied, the angle α between the z and M is determined by the pulse's strength (B_1) and duration (τ).

$$\alpha = \gamma B_1 \tau$$

Equation 1.3: Tip Angle

Once the RF pulse is turned off three things occur. First, the magnetization vector continues to precess around the z-axis at the Larmour frequency. The rotating magnetization induces an electromagnetic force in a radiofrequency receiver coil. The signal measured is

known as a free induction decay (FID) curve and is the basic NMR signal that is recorded
(53).
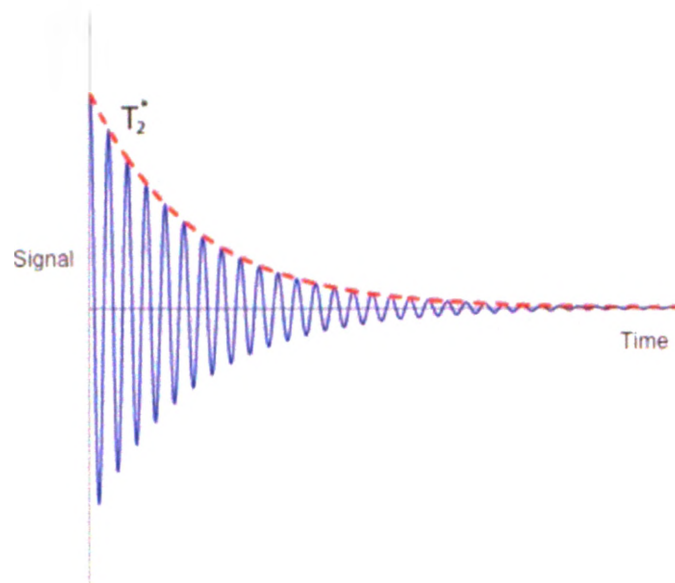
Figure 1.6: FID Curve of a Sample

Second, the magnetization begins to return to its original position along M_z and third, the
protons that were precessing in phase with each other begin to dephase. The last two
characteristics are known as relaxation effects and are a source of contrast within MR images
(56). Another source of contrast is the proton density of the tissue.

To spatially locate the NMR signal, magnetic field gradients are employed that
linearly change the local magnetic field. MR images are then created with pulse sequences.
A pulse sequence is a series of software controlled manipulations of the MR hardware to
apply different RF and gradient pulses to the sample of interest. The strength, duration, and
frequency of the different pulses capture the differences in the relaxation times in the sample
and create the contrast seen in MR images. The next sections will expand on these concepts
of MR imaging.

1.2.3 Relaxation

Relaxation effects begin immediately after the RF pulse is turned off. The first of these effects is known as T1 relaxation. The protons in the sample absorb energy from the applied RF pulse. Once the RF pulse is turned off the absorbed energy is released into the surroundings, or the spin-lattice. T1 relaxation characterizes the return of the net magnetization to its equilibrium state along the z-axis. The T1 relaxation time is a time constant defined as the time it takes the magnetization along the z-axis (M_z) to reach $0.63M_0$ following a RF excitation pulse (56). It is also known as the spin-lattice time constant.
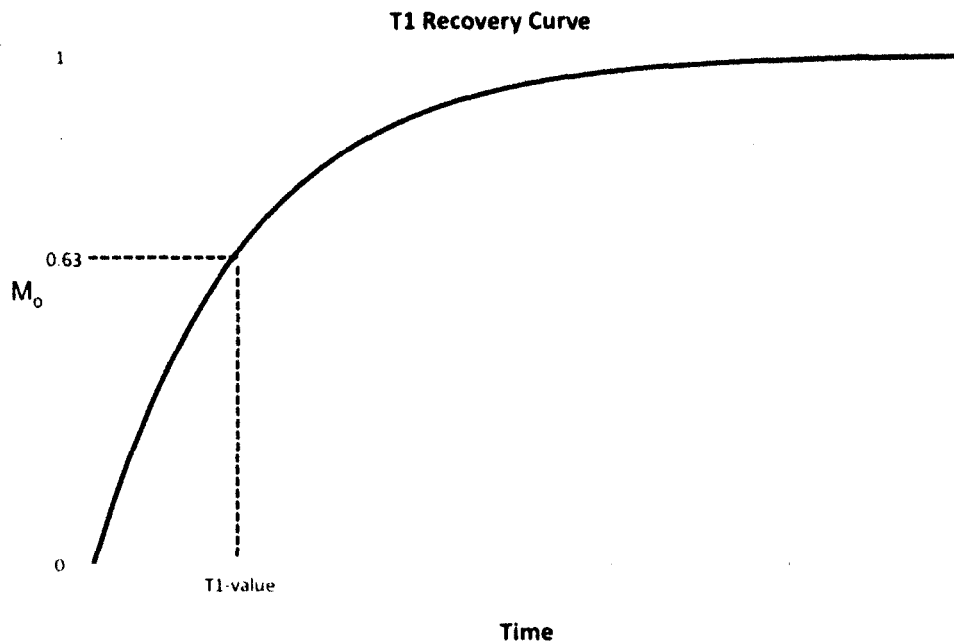
T1 Recovery Curve

Figure 1.7: T1 Recovery Curve After a 90° Pulse

M_z can be found using the following equation (53):

$$M_z = M_o + [M_z(0) + M_o]e^{-t/T1}$$

Equation 1.4: T1 Recovery

Following a 90° pulse M_o is completely tipped into the transverse plane i.e. $M_z(0) = M_o$ and equation 1.4a becomes (53):

$$M_z = M_o + (1 - e^{-t/T1})$$

Equation 1.5: T1 Recovery After 90° Pulse

Another source of relaxation occurs in the transverse plane. T2 relaxation is characterized by a loss of phase coherence of the spins. As the net magnetization precesses in the transverse plane each individual spin begins to precess at a different Larmour frequency. The longer the magnetization is allowed to precess the greater the phase difference between the individual spins. As the spins dephase in the transverse plane their signals begin to cancel each other out leading to a loss of net signal. The T2 relaxation time, or spin-spin relaxation, is a time constant used to describe when M_{xy} has lost (or dephased to) 63% of its initial value (56).

T2 Relaxation Curve
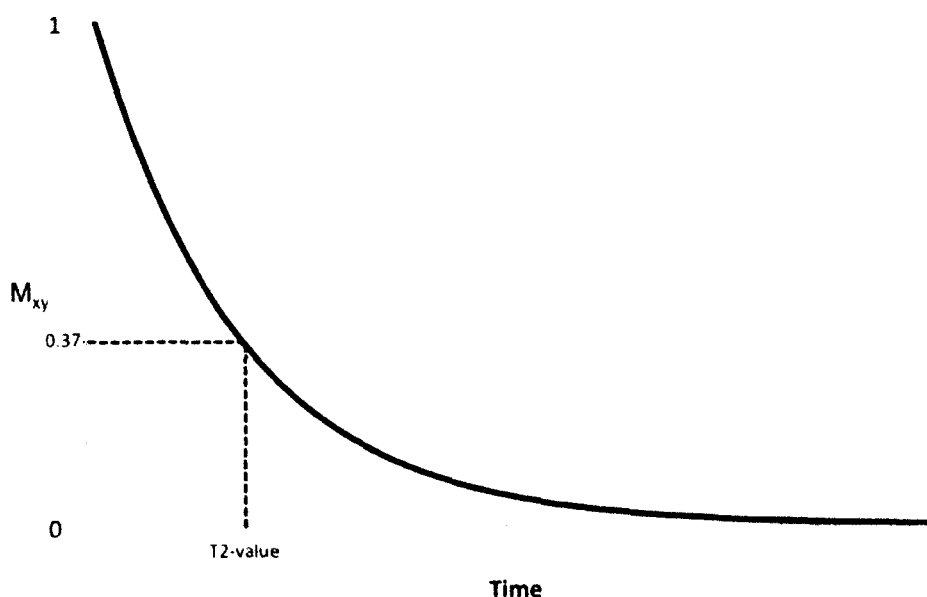
Figure 1.8: T2 Relaxation Curve After a 90° Pulse

Loss of signal in the transverse plane due T2 relaxation is given by (53):

$$M_{xy} = M_{xyo}e^{-t/T2}$$

Equation 1.6: T2 Recovery

If the RF applied is a 90° pulse then $M_{xyo}=M_o$.

This relaxation effect is caused by two sources. One is the energy exchange between molecules through vibrations and/or rotations. This source is known as true spin-spin relaxation (T2). The second is due to magnetic field inhomogeneities (T2') (57). Magnetic field inhomogeneities are caused by variations in the static magnetic field $B_\varnothing$, in the sample

15

itself where different magnetic susceptibilities change the local magnetic field at tissue boundaries. Thus the total transverse relaxation (T2*) is given by (58):

$$\frac{1}{T2*} = \frac{1}{T2} + \frac{1}{T2'}$$

Equation 1.7: Components of T2 Relaxation

T2 effects are not reversible and cause a permanent loss in the magnitude of M_{xy}. However some T2' effects can be refocused with different pulse sequences.

1.2.4 Spatial Encoding

Spatial encoding in MRI is performed using gradients. Magnetic field gradients are generated with gradient coils, which consist of two coils each carrying a current of opposite direction to each other. Each coil creates a magnetic field that decreases with distance. When these magnetic fields are added to the main magnetic field Bø, Bø will no longer be uniform and instead would be changing linearly (56). This in turn causes a change in the local magnetic field and the protons within a sample will spin with a slightly different Larmour frequency depending on their location in the sample. Each axis has its own set of gradients so all three axies can be spatially encoded. There is a slice select, frequency encoding, and phase encoding gradient. As a result of these gradients, the signal from each location of the sample will have a different frequency and phase.

Typically slice selection is chosen in the z-axis but all three spatial encoding techniques can be used in any axis. The slice of interest is selected by applying an RF pulse in conjunction with a slice select gradient. The frequency of the RF pulse corresponds to the

Larmour frequency of the location of interest, which as mentioned above changes linearly in the sample because of the applied gradient. When the RF pulse is applied, only those protons with the Larmour frequency that matches the frequencies in the RF pulse will be tipped in the transverse plane (55). All frequencies outside the RF bandwidth will not be excited and will not produce a signal. By defining the bandwidth of the RF pulse to be a certain range of frequencies, the thickness of the slice can also be defined. Decreasing the bandwidth of the RF pulse or increasing the gradient amplitude can decrease slice thickness (53). The application of the gradient during the RF pulse helps define a slice but also causes M_{xy} to dephase once it is in the transverse plan. Therefore following the pulse another gradient is applied in the reverse direction to refocus the magnetization.

1.2.4.1 Frequency Encoding

Frequency encoding typically occurs in the x-axis. The application of the frequency encoding gradient causes protons in the sample to spin at different frequencies. The different frequencies exhibited by the protons in the sample is proportional to its location. The frequency of a proton at a particular location is described by (53):

$$v = \gamma(B_o + xG_x)$$

Equation 1.8: Frequency of a Proton as a Function of Location

Where x is the location of the measurement and G_x is the gradient strength. The frequency encoding gradient remains turned on while the data is being acquired.

1.2.4.2 Phase Encoding

Phase encoding is the final method of spatial encoding and typically occurs in the y-axis. Phase refers to the angle M_{xy} makes with the reference axis (55). This change in phase is created in the same manner that frequency variations are. The difference is the duration of the gradient pulses. In the frequency encoding gradient remains on during the entire time the signal is being acquired but the phase encode gradient is turned on only temporarily. So once the phase gradient is turned off the spins are be precessing at the same rate as before the pulse but the spins are now be at different positions, or have a difference phase. The amount of phase shift depends on the magnitude and the duration of the phase encoding gradient. The phase encoding gradient is also the only gradient that increases in amplitude (56). This phase difference can be related to the location of the measurement. After the implementation of the three spatial encoding gradients the resulting signal from each location has a unique frequency and phase. This time dependent signal can then be processed using a mathematical technique known as the Fourier transform. The Fourier transform takes a signal in the time domain and decomposes it into its frequency components. The MR image can then be reconstructed using the data in the time (or spatial frequency) domain by using an inverse Fourier transform (54).

1.2.5   MRI Pulse Sequences

MRI pulse sequences are used to manipulate the relaxation effects of the protons to generate the contrast needed. One of the most widely used pulse sequences is the spin echo (SE) sequence. SE sequences consists of one 90° pulse and at least one 180° pulse (55). The initial 90° RF pulse is applied to the sample and is followed by the spatial encoding

gradients. If the sample were to be read at this point the signal generated would be very low due to the dephasing effects from intrinsic factors and the gradients. At a time TE/2, where TE is the echo time, the 180° RF pulse is applied along the x'-axis. This pulse flips the spins around the x'-axis (53). Now the effects that were causing the spins to dephasing are causing them to rephase and at forming an echo at time TE.

Immediately after the 90° pulse   Immediately after the 180° pulse   Formation of the spin echo
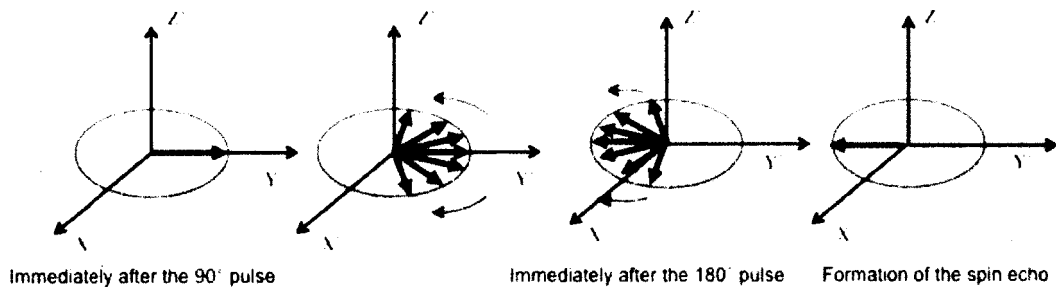
Figure 1.9: Formation of Spin Echo

The 180° pulse refocuses all T2' effects making SE sequences robust against susceptibility differences. The contrast produced by SE sequences is dependent on the timing parameters. The timing diagram of the most basic SE is shown below. The sequence is repeated after a time TR, which is known as the repetition time.
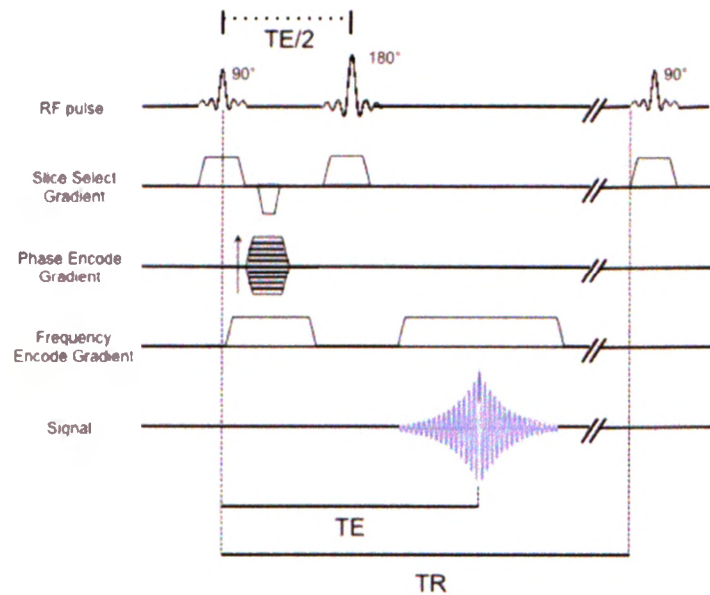
Figure 1.10: Spin Echo Pulse Sequence

Another basic MRI pulse sequence is the gradient echo (GRE) pulse sequence. GRE sequences are used to refocus the magnetization after accruing phase due to the spatial encoding gradients. This can be accomplished by applying a gradient of the same strength and duration but with opposite polarity. The dephasing due to the spatial gradients is then reversed and the spins will once again rephase and form an echo (53). Gradient echo sequences do not correct dephasing of the spins due to field inhomogeneities, other than those caused by the magnetic field gradients. This results in a smaller signal from GRE sequences compared to those from a SE sequence of an identical sample at the same TE. A timing diagram of the most simple of GRE sequences is shown below.
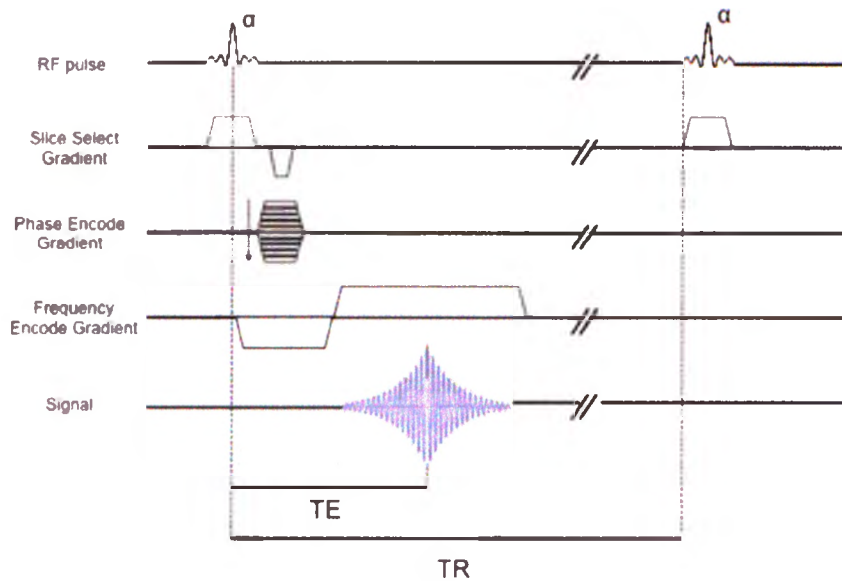
Figure 1.11: Gradient Echo Pulse Sequence

A RF pulse is applied in conjunction with a slice select gradient and tips the magnetization by an angle α. GRE typically uses tip angles $< 90°$, which enables faster imaging compared to SE sequences since full T1 relaxation is not required before the sequence can be repeated. A slice refocusing gradient is applied after the RF pulse along with the phase and frequency encoding gradients. The frequency encoding gradient is used to completely dephase the magnetization such that maximum coherence is achieved when the second frequency encoding (readout) gradient is applied. At time TE an echo will be formed and the signal will be measured.

Steady-state free precession (SSFP) in magnetic resonance was first described by Herman Carr in 1958 (59). SSFP describes the behaviour of the net magnetization when the same RF pulse is repeatedly applied to the sample at regular time intervals. An initial RF pulse tips the magnetization an angle α. If the same RF is applied then the magnetization will be tipped back at an angle that is slightly larger that α since full T1 recovery did not

occur. If the process is repeated with a RF pulse of the same magnitude and the duration between pulses remains at a constant TR, then eventually the amount of magnetization relaxation during TR will equal the amount of magnetization tipped after excitation. Since there are both longitudinal and transverse components present during the signal acquisition the signal itself is dependent on T2/T1 (60). Balanced-SSFP sequences also offer the highest signal-to-noise (SNR) ratio per unit time of any pulse sequence.

Three conditions must be met before the steady-state condition can occur. One is that is that TR<<T2<T1. This limits the amount of T1 recovery and dephasing effects due to intrinsic T2. The second is that all dephasing effects must be the same between each RF pulse and lastly α and TR must remain constant (61). The timing diagram below shows the pulse sequence of a b-SSFP sequence.
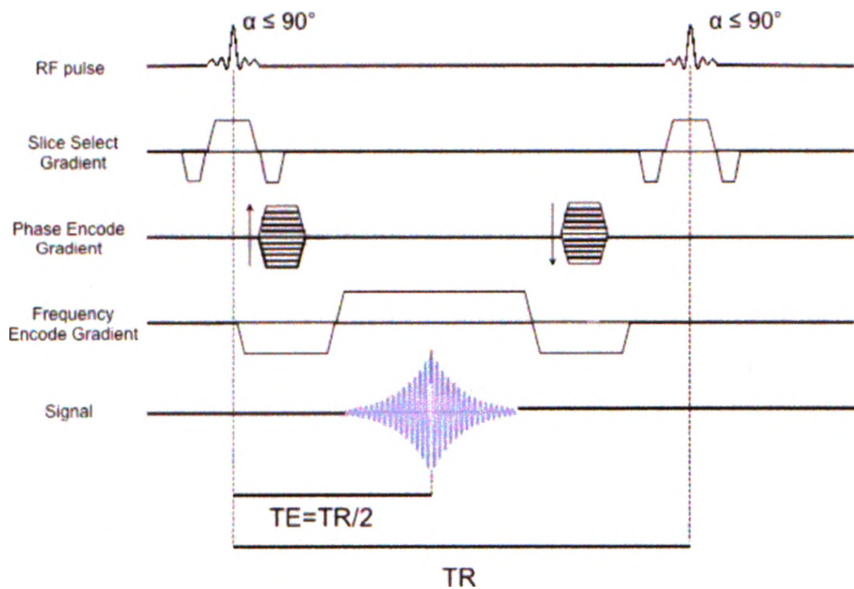
Figure 1.12: b-SSFP Pulse Sequence

In the timing diagram it can be seen that a RF pulse is applied with a tip angle α after which the spatial encoding gradients are applied. After several TR periods (~5T2/TR) the

22

magnetization will be in steady-state and data acquisition will begin (61). In this sequence all three gradients are refocused or "balanced". This is the difference between b-SSFP and SSFP sequences. SSFP sequences do not refocus the dephasing effects due to the frequency encoding gradient and the net magnetization before the next RF pulse is zero. The net magnetization for b-SSFP at the beginning of the sequence until the next RF pulse is nearly identical with the exception of small T1 and T2 effects occurring during TR (60).

1.2.6 Contrast Agents

MRI contrast agents differ from agents used in other imaging modalities in that it is not the contrast agent itself being imaged, rather it is the effect of the contrast agent on the surrounding tissues. There are two major classes of MR contrast agents: paramagnetic and superparamagnetic. All contrast agents shorten both T1 and T2 times of the surrounding tissues. However on a percentage basis most contrast agents affect one relaxation time more than the other. A T1 contrast agent is one that induces T1 recovery significantly more than T2 dephasing and vice versa for T2 agents (62).

The first MRI contrast agents developed were paramagnetic contrast agents, which are also called T1-shortening agents. Most T1-shortening agents are gadolinium-based, although there are some agents that are manganese-based (63-66). At seven, gadolinium has the most unpaired electrons of any of the lanthanide metals creating a large magnetic moment (67). Gadolinium itself is toxic to the body and has to be linked to a chelating agent that can be eliminated by the body through normal renal functions. This chelating agent also helps surrounding water interact with the gadolinium atom to induce T1 relaxation (62). Paramagnetic agents induce T1 relaxation by transferring energy to the lattice. This

stimulates the protons in the higher energy state to release energy to return to the lower energy state and leads to recovery of M_z (56). This T1 shortening equates to a bright signal on T1 weighted images (67). There are multiple T1 shortening contrast agents available for clinical use and include: Magnevist® (gadopentetate dimeglumine [Gd-DTPA]), Multihance® (gadobenate dimeglumine [Gd-BOPTA]), Gadovist® (Gadbutrol), and Omniscan® (gadodiamide) (68).

Superparamagnetic contrast agents all consist of an iron-oxide core. These agents are usually T2-shortening agents, although some can also be used as a T1 shortening agent. When these superparamagnetic iron-oxide (SPIO) contrast agents are placed within a sample the large magnetic moment caused by the external magnetic field induces local magnetic field gradients causing protons in the vicinity of the contrast agent to experience a different frequency than the protons further away from the contrast agent. This results in a faster dephasing, or a T2 shortening of the surrounding protons, and a loss of signal. Pulse sequences that are T2 or T2* weighted are used to exploit this phenomenon and the area at and surrounding the contrast agent appears as a region of hypointensity, or signal loss (69). The part of the SPIO particle that is responsible for producing contrast is the crystallites of iron-oxide that are located in the particle's core. The crystallite consists of magnetite ($Fe_2^{3+}O_3Fe^{2+}O$) and has its own magnetic domain (69). These crystallites are then packed together to form one crystal. Without an external magnetic field the magnetic domains are randomly oriented but align in the same direction in the presence of an external magnetic field. SPIO particles consist of many crystals stabilized with a coating (70).

SPIO particles are classified according to their hydrodynamic diameter, which is the total diameter of the particle (iron-oxide core and the coat). The hydrodynamic diameters of

ultrasmall SPIO (USPIO, generic name Combidex®), SPIO (generic name Feridex® or Endorem®), and micron-sized SPIO (MPIO) are roughly 10-40 nm, 80-150 nm, and 0.9-8.5μm respectively (68, 71). Monocystalline (MION), cross-linked iron-oxide (CLIO) and anionic iron-oxide (AMNP) nanoparticles are also used as MRI contrast agents. Contrast agents have aided in the identification and characterization of tumors in humans.

1.2.7 Cancer and MRI

The discovery that cancer tissue had different relaxation rates compared to normal tissue revealed a property by which tissues could be differentiated using magnetic resonance (72). Since then MRI has played an important role in the detection, staging, and the characterization of cancer. The spread of cancer to the muscle of the bladder (73), the myometrium (the middle layer) of the uterus (73) and the perineural spread of malignancies at the skull base (74) are all indicators of a poor prognosis and can confidently be diagnosed with MRI due to its ability to generate superior soft tissue contrast.

The value of MRI in the early detection of breast cancer has just recently been highlighted. Many studies have compared MRI with mammography in the screening for breast cancer in high-risk patients. All have found that MRI was significantly more sensitive than mammography for detecting abnormalities in the breast. Overall the studies showed that sensitivity of MRI and mammography was between 71-100% and 16-40%, (75) respectively. This led the American Cancer Society to update its guidelines in 2007 to recommend a MRI scan with mammography when screening patients with a high risk for breast cancer (75).

A murine model of metastatic melanoma has shown that the T2 value of diseased bone marrow was significantly longer than that of normal bone marrow. This has shown that bone metastasis could be identified with MRI before the loss of bone (76). The liver is a common site of metastasis and MRI is recommended for staging and characterizing lesions in the liver (77). This is especially important since benign lesions, such as hepatic cysts and hemangiomas, are common in the liver. It has been found that there is less signal from liver metastases when compared to benign lesions on T2 weighted images. Thus hemangiomas and metastatic growths can be differentiated when using a multi-echo T2-weighted sequence because the signal from the tumor will get progressively less while the benign lesions remain the same (78, 79). SPIO contrast agents have also been used to detect hepatic metastases between 2-3 mm (80). The lymph nodes are also a common site for metastasis. Lymph node metastases, like liver metastasis, can be detected using SPIO contrast agents (52, 81, 82). Cellular MRI has made the detection of metastatic lesions in these two tissues possible.

1.3 Cellular MRI

Cellular MRI has been referred to as the non-invasive and repetitive imaging of targeted cells and cellular processes in living organisms (83). Cellular MRI techniques have been used to study stem cells (84, 85), pancreatic islets (86), cancer cells (87, 88), inflammatory cell infiltration (89-91), and dendritic cells (92).

The sensitivity of cellular MRI techniques has advanced to the point where a single cell can be imaged in-vivo (48). Two requirements are needed for successful cellular MR imaging; high resolution scanning and contrast enhancement of the cells. This need for high resolution has been an instigator for high field scanners. Most cellular MRI experiments are

performed on 4.7T or higher. Specially designed hardware, specifically gradient and RF coils, has allowed high resolution scanning to be performed at clinical field strengths. Clinical scanners alone have the ability to reproduce a resolution of up to 250 μm and high field small animal scanners can produce higher resolution scans of ~50 μm. However this is still inadequate to resolve a single cell, which is approximately 10 μm in diameter.

There is also a need to differentiate between the cells of interest and the surrounding tissues. For this reason contrast agents must be implemented to increase the detectibility of these cells. The vast majority of cell labeling is performed with SPIO agents. Iron-oxide has greater relaxivity effects than that of gadolinium contrast agents. At 0.47T, Magnevist has relaxivity values of 6 mmol^{-1}s^{-1} and 4 mmol^{-1}s^{-1} for T2 and T1 compared to a T2 relaxivity of 100 mmol^{-1}s^{-1} and a T1 relaxivity of 30 mmol^{-1}s^{-1} for a typical SPIO agent at the same field strength (70). This means that many more gadolinium molecules are required to be internalized by cells to obtain the same relaxivity effects produced by iron particles. It has also been shown that the gadolinium molecules can detach from the chelating molecule and become toxic to the cell (93), while iron is stored naturally in the body. Thus SPIO are the contrast agents of choice for cell labeling.

SPIO contrast agents have been used for active cell labeling. Active labeling employs an intravenous injection of contrast agent that is meant to be taken up by phagocytic cells, labeling them in-vivo. This type of labeling is especially effective for studying diseases and/organs which involve phagocytic immune cells. The immune cells become labeled in-vivo and migrate to the site of disease, and the appearance of hypointensity in the MR image provides information about the presence of these cells. An animal model of multiple sclerosis (MS) is the autoimmune encephalomyelitis (EAE). Using an active labeling

approach, macrophages in brain lesions in an EAE model were identified using IV administered SPIO (90).

Active labeling with SPIO is also the approach that has been used to detect metastasis in the lymph nodes and liver. After the injection of intravenous USPIO, nodes with metastases have heterogeneous contrast within the nodes. The dark areas are a result of uptake of iron by normal node tissue which contains phagocytic immune cells, while cancer cells within the nodes appear bright in comparison (94). A study with 33 breast cancer patients demonstrated 94% accuracy in detecting metastases in the axillary lymph nodes using USPIO (95).

Imaging metastasis in the liver works on the same principle. The Kupffer cells (macrophages in the liver) phagocytose SPIO particles after their IV administration. Since the tumor tissues lack Kupffer cells, they will appear bright against the hypointense background of normal liver. Active labeling has also been used to study macrophage infiltration in stroke (96), arthritis (91), transplanted organs (97, 98) and spinal cord injury (89).

Ex-vivo prelabeling of cells involves incubating the contrast agent and cells in a plate with media for 2-24 hours before injecting the cells in-vivo. The amount of contrast agent taken up by cells is dependent on the cell type, contrast agent type and the concentration of the contrast agent. Simple incubation is often not effective at labeling non-phagocytic cells with sufficient amounts of iron to allow their detection by MRI. For example, it has been shown that mesenchymal stem cells and HeLa cells do not take up native SPIO particles after 24-48 hours of incubation (99). Methods, like electroporation (100), have been utilized to increase the in non-phagocytic cells. The linking of SPIO particles to the HIV tat peptide

has been shown to increase transport of iron into lymphocytes (101). The use of transfection agents such as protamine sulphate and poly-L-lysine (PLL) has also been shown to increase iron uptake. Iron particles coated with a transfection agent can chaperon the particle into the cell. Iron uptake in mesenchymal stem cells, mouse lymphocytes, rat oligodendrocytes and HeLa cells increased between 2-70 times when SPIO particles were coated with PLL compared to an incubation of bare SPIO particles (102). Most cells will take up MPIO particles readily without the need for transfection agents.

Several factors contribute to the choice of SPIO or MPIO contrast agents for cell tracking. SPIO have coatings that are dextran based making them biodegradable. They are FDA approved (in the USA) and should make for an easier transition from the lab to the clinic. There are several potential advantages of using MPIO for tracking cancer cells. MPIO particles are coated with a synthetic polymer making them inert and unsuitable for clinical use. This inert property of MPIO can be advantageous when tracking rapidly dividing cells. The size of the iron core in MPIO particles is much larger than that of SPIO and contains more iron. Therefore a smaller number of MPIO particles are needed for detection. For example, Bangs laboratories produce MPIO particles that have a hydrodynamic diameter of 0.9 μm and a magnetite core with a diameter of 760 nm while SPIO particles has a magnetite core with a diameter of ~10 nm. This difference in iron content translates to decreased T2 relaxivity values for Bangs beads when compared to SPIO. At 4.7T, the T2 values of Bangs beads and SPIO particles are 356 mmol^{-1}s^{-1} and 240 mmol^{-1}s^{-1} respectively (103). It has been demonstrated that a single MPIO bead can be imaged in-vivo (104). In our work we have utilized MPIO particles for our cell labeling for all of these reasons.

Dilution of the transient contrast agent is always a concern when imaging labeled cells. To overcome this limitation targeted contrast agents have been developed. Ligands, antibodies and molecules have been conjugated to MR contrast agents to target certain cells for cell labeling. Amino acids, especially glutamine, are required for cell proliferation. Gadolinium chelates conjugated to glutamate residues have been developed as a targeted MR contrast agent for cancer. After an intravenous injection of the contrast agent, tumors from neuroblastoma cells in normal mice and in Her2/neu transgenic mice which developed mammary carcinomas could be visualized (105). Many cancer cells express an increased up take in folic acid. USPIO conjugated to folic acid are preferentially taken up by HeLa cells but not by osteosarcoma cells without the folate receptor (106). CD20 is a protein that is expressed on mature B-cells, lymphoma cells, and melanoma cells. USPIO conjugated to an anti-CD20 antibody was shown to target lymphoma cells injected into nude mice resulting in a decrease in signal within the tumor (107). One of the challenges when using targeted contrast agents is specificity. While cancer cells over express some molecules or receptors, normal cells can also express these markers, which can make the identification of cancer cells difficult. Therefore cells have been engineered that contain reporter genes that can sequester iron within the body.

MagA is a gene in magnetotactic bacteria that is involved in iron transport and creates magnetosomes that act like iron-based contrast agents creating signal loss in MRI images. Recently human cells have been transfected with MagA and showed a 3-4 fold decrease in T2 in MR images compared to normal cells (108). Ferritin has also been implemented as a transgene reporter (109).

1.4 Overview and Hypothesis

The metastasis through the lymphatic system needs to be better characterized. It has been less studied when compared to metastasis through the circulatory system. Yet disease in the lymph nodes is also associated with a poorer prognosis in cancer patients. MRI is a tool that can offer more insight into this dynamic process than traditional end-point examinations using histological analysis. Lymphatic metastasis has been studied with MRI. MRI has been able to detect metastatic tumors within lymph nodes using both iron and gadolinium based contrast agents (52, 81, 110-112). However the tracking of the cells themselves has never been attempted.

The <u>main hypothesis</u> of this project is that MRI can be used to detect metastatic cancer cells in the mouse lymphatic system.

To test this hypothesis several questions needed to be addressed including whether or not MPIO has any effect on the function or viability of B16F10 cells. A good mouse model of metastatic cancer in the lymphatics was also required. The second chapter addresses these questions by comparing the metastatic potential of labeled and unlabeled cells in two different injection sites. A commonly used subcutaneous injection of B16F1 cells into the flank of a mouse was compared with a novel model developed by collaborators at Becton Dickinson Technologies that involves an injection of cells directly in the lymph node of the mouse. The specific hypotheses were that MPIO particles would not affect the growth rate or metastatic potential of the B16F10 cells and that the direct intranodal injection of cells would result in more metastases in the lymph nodes.

Chapter 3 focuses on imaging. Using the intranodal model of metastasis we imaged mice longitudinally to address our main hypothesis and to determine the feasibility of

detecting metastatic cancer cells that have migrated to a distant lymph node. Samples were also analyzed histologically and with inductively coupled plasma mass spectrometry. This work was presented in an oral presentation at the 16th annual ISMRM in 2008 in Toronto, Canada and will be submitted for publication.

In Chapter 4 a pilot study is presented where an additional model system was evaluated. B16F10 cells were implanted in the mammary fat pad, a site that if often used for breast cancer studies. The goal was to produce metastasis in the inguinal lymph node which is one of the most easily visualized in the mouse. Here we conducted a similar experiment to that described in Chapter 2 where the comparison of the metastatic potential of labeled and unlabeled cells at the implant site was made. Also, two different cell counts were used. In this experiment a small subset of animals were also imaged longitudinally.

1.5 References

1. Stacker SA, Achen MG, Jussila L, Baldwin ME, Alitalo K. Lymphangiogenesis and cancer metastasis. Nat Rev Cancer. 2002 Aug;2(8):573-83.

2. Gupta GP, Massague J. Cancer metastasis: Building a framework. Cell. 2006 Nov 17;127(4):679-95.

3. Carter RL. Some aspects of the metastatic process. J Clin Pathol. 1982;35:1041-9.

4. Chambers AF, Groom AC, MacDonald IC. Dissemination and growth of cancer cells in metastatic sites. Nat Rev Cancer. 2002 Aug;2(8):563-72.

5. Townson JL, Chambers AF. Dormancy of solitary metastatic cells. Cell Cycle. 2006 Aug;5(16):1744-50.

6. Aguirre-Ghiso JA. Models, mechanisms and clinical evidence for cancer dormancy. Nat Rev Cancer. 2007 Nov;7(11):834-46.

7. Luzzi K, MacDonald IC, Schmidt EE, Kervliet N, Morris VL, Chambers AF, et al. Multistep nature of metastatic inefficiency: Dormancy of solitary cells after successful extravasation and limited survival of early micrometastasis. Am. J. Pathol. 1998;153(3):865.

8. Paget S. The distribution of secondary growths in cancer of the breast. The Lancet. 1889;1:99-101.

9. Poste G, Doll J, Hart IR, Fidler IJ. In vitro selection of murine B16 melanoma variants with enhanced tissue-invasive properties. Cancer Res. 1980 May;40(5):1636-44.

10. Hart IR, Fidler IJ. Role of organ selectivity in the determination of metastatic patterns of B16 melanoma. Cancer research. 1980;40:2281-7.

11. de la Monte SM, Moore GW, Hutchins GM. Nonrandom distribution of metastases in neuroblastic tumors. Cancer. 1983 Sep 1;52(5):915-25.

12. Saitoh H, Yoshida K, Uchijima Y, Kobayashi N, Suwata J, Kamata S. Two different lymph node metastatic patterns of a prostatic cancer. Cancer. 1990 Apr 15;65(8):1843-6.

13. Rose PG, Piver MS, Tsukada Y, Lau TS. Metastatic patterns in histologic variants of ovarian cancer. an autopsy study. Cancer. 1989 Oct 1;64(7):1508-13.

14. Weiss L. Comments on hematogenous metastatic patterns in humans as revealed by autopsy. Clin Exp Metastasis. 1992 May;10(3):191-9.

15. McDowell J, Windelspecht M. The lymphatic system. Westport, CT: Greenwood Press; 2004.

16. Swartz MA, Skobe M. Lymphatic function, lymphangiogenesis, and cancer metastasis. Microsc Res Tech. 2001 Oct 15;55(2):92-9.

17. Nathanson SD. Insights into the mechanisms of lymph node metastasis. Cancer. 2003 Jul 15;98(2):413-23.

18. Essner R. Experimental frontiers for clinical applications: Novel approaches to understanding mechanisms of lymph node metastases in melanoma. Cancer Metastasis Rev. 2006 Jun;25(2):257-67.

19. Padera TP, Kadambi A, di Tomaso E, Carreira CM, Brown EB, Boucher Y, et al. Lymphatic metastasis in the absence of functional intratumor lymphatics. Science. 2002 Jun 7;296(5574):1883-6.

20. Oliver G, Detmar M. The rediscovery of the lymphatic system: Old and new insights into the development and biological function of the lymphatic vasculature. Genes Dev. 2002;16(9):773-83.

21. Nagata H, Arai T, Soejima Y, Suzuki H, Ishii H, Hibi T. Limited capability of regional lymph nodes to eradicate metastatic cancer cells. Cancer Res. 2004 Nov 15;64(22):8239-48.

22. Shields JD, Fleury ME, Yong C, Tomei AA, Randolph GJ, Swartz MA. Autologous chemotaxis as a mechanism of tumor cell homing to lymphatics via interstitial flow and autocrine CCR7 signaling. Cancer Cell. 2007 Jun;11(6):526-38.

23. Gershenwald JE, Fidler IJ. Cancer. targeting lymphatic metastasis. Science. 2002 Jun 7;296(5574):1811-2.

24. Landry CS, McMasters KM, Scoggins CR. The evolution of the management of regional lymph nodes in melanoma. J Surg Oncol. 2007 Sep 15;96(4):316-21.

25. Canadian Cancer Society/National Cancer Institute of Canada. Canadian cancer statistics 2007. Toronto, Canada: 2007.

26. Bressac-de-Paillerets B, Avril MF, Chompret A, Demenais F. Genetic and environmental factors in cutaneous malignant melanoma. Biochimie. 2002 Jan;84(1):67-74.

27. Armstrong BK, Kricker A. How much melanoma is caused by sun exposure? Melanoma Research. 1993;3:395-401.

28. Homsi J, Kashani-Sabet M, Messina JL, Daud A. Cutaneous melanoma: Prognostic factors. Cancer Control. 2005 Oct;12(4):223-9.

29. Gershenwald JE, Thompson W, Mansfield PF, Lee JE, Colome MI, Tseng CH, et al. Multi-institutional melanoma lymphatic mapping experience: The prognostic value of sentinel lymph node status in 612 stage I or II melanoma patients. J Clin Oncol. 1999 Mar;17(3):976-83.

30. Scolyer RA, Murali R, Gershenwald JE, Cochran AJ, Thompson JF. Clinical relevance of melanoma micrometastases in sentinel nodes: Too early to tell. Ann Oncol. 2007 Apr;18(4):806-8.

31. Teicher BA. Tumor models in cancer research. Totowa, N.J.: Humana Press; 2002.

32. Fidler IJ. Selection of successive tumor lines for metastasis. Nat New Biol. 1973 Apr 4;242(118):148-9.

33. Brunson KW, Nicolson GL. Selection of malignant melanoma variant cell lines for ovary colonization. J Supramol Struct. 1979;11(4):517-28.

34. Brunson KW, Beattie G, Nicolsin GL. Selection and altered properties of brain-colonising metastatic melanoma. Nature. 1978 Apr 6;272(5653):543-5.

35. Shrayer DP, Bogaars H, Wolf SF, Hearing VJ, Wanebo HJ. A new mouse model of experimental melanoma for vaccine and lymphokine therapy. Int J Oncol. 1998 Aug;13(2):361-74.

36. Nathanson SD, Haas GP, Mead MJ, Lee M. Spontaneous regional lymph node metastases of three variants of the B16 melanoma: Relationship to primary tumor size and pulmonary metastas. J Surg Oncol. 1986;33(1):41-5.

37. Wunderbaldinger P, Josephson L, Bremer C, Moore A, Weissleder R. Detection of lymph node metastases by contrast-enhanced MRI in an experimental model. Magn Reson Med. 2002 Feb;47(2):292-7.

38. Alterman AL, Stackpole CW. B16 melanoma spontaneous brain metastasis: Occurrence and development within leptomeninges blood vessels. Clin Exp Metastasis. 1989 Jan-Feb;7(1):15-23.

39. Fidler IJ, Nicolson GL. Tumor cell and host properties affecting the implantation and survival of blood-borne metastatic variants of B16 melanoma. Isr J Med Sci. 1978 Jan;14(1):38-50.

40. Foster PJ, Dunn EA, Karl KE, Snir JA, Nycz CM, Harvey AJ, et al. Cellular magnetic resonance imaging: In-vivo imaging of melanoma cells in lymph nodes of mice. Neoplasia. 2008 Mar;10(3):207-16.

41. Presnell JK, Schreibman MP, Humason GL. Humason's animal tissue techniques. 5th ed. Baltimore: Johns Hopkins University Press; 1997.

42. Bergman RA, Afifi AK, Heidger PM. Histology. Philadelphia: Saunders; 1996.

43. Lewis JD, Destito G, Zijlstra A, Gonzalez MJ, Quigley JP, Manchester M, et al. Viral nanoparticles as tools for intravital vascular imaging. Nat Med. 2006 Mar;12(3):354-60.

44. Hyafil F, Cornily JC, Feig JE, Gordon R, Vucic E, Amirbekian V, et al. Noninvasive detection of macrophages using a nanoparticulate contrast agent for computed tomography. Nat Med. 2007 May;13(5):636-41.

45. Gambhir SS. Molecular imaging of cancer with positron emission tomography. Nat Rev Cancer. 2002;2:685-93.

46. Graham KC, Wirtzfeld LA, MacKenzie LT, Postenka CO, Groom AC, MacDonald IC, et al. Three-dimensional high-frequency ultrasound imaging for longitudinal evaluation of liver metastases in preclinical models. Cancer Res. 2005 Jun 15;65(12):5231-7.

47. Wirtzfeld LA, Wu G, Bygrave M, Yamasaki Y, Sakai H, Moussa M, et al. A new three-dimensional ultrasound microimaging technology for preclinical studies using a transgenic prostate cancer mouse model. Cancer Res. 2005 Jul 15;65(14):6337-45.

48. Heyn C, Ronald JA, Mackenzie LT, MacDonald IC, Chambers AF, Rutt BK, et al. In-vivo magnetic resonance imaging of single cells in mouse brain with optical validation. Magn Reson Med. 2006 Jan;55(1):23-9.

49. Shapiro EM, Sharer K, Skrtic S, Koretsky AP. In-vivo detection of single cells by MRI. Magn Reson Med. 2006 Feb;55(2):242-9.

50. Deroose C, Abhijit D, Loening AM, Chow PL, Ray P, Chatzioannou AF, et al. Multimodality imaging of tumor xenografts and metastases in mice with combined small-animal PET, small-animal CT, and bioluminescence imaging. J Nucl Med. 2007;48:295-303.

51. Winkelmann CT, Figueroa SD, Rold TL, Volkert WA, Hoffman TJ. Microimaging characterization of a B16-F10 melanoma metastasis mouse model. Mol Imaging. 2006 Apr-Jun;5(2):105-14.

52. Choi SH, Moon WK, Hong JH, Son KR, Cho N, Kwon BJ, et al. Lymph node metastasis: Ultrasmall superparamagnetic iron oxide-enhanced MR imaging versus PET/CT in a rabbit model. Radiology. 2007 Jan;242(1):137-43.

53. Nishimura DG. Principles of magnetic resonance imaging. United States of America: Dwight G. Nishimura; 1996.

54. Pykett IL, Newhouse JH, Buonanno FS, Brady TJ, Goldman MR, Kistler JP, et al. Principles of nuclear magnetic resonance imaging. Radiology. 1982 Apr;143(1):157-68.

55. Haacke EM. Magnetic resonance imaging: Physical principles and sequence design. New York: J. Wiley-Liss; 1999.

56. Brown MA, Semelka RC. MRI: Basic principles and applications. 1st ed. United States of America: Wiley-Liss Inc.; 1995.

57. Smith RC, Lange RC. Understanding magnetic resonance imaging. USA: CRC Press; 1997.

58. Ma J, Wehrli FW. Method for image-based measurement of the reversible and irreversible contribution to the transverse-relaxation rate. J Magn Reson B. 1996 Apr;111(1):61-9.

59. Carr HY. Steady-state free precession in nuclear magnetic resonance. Phys. Rev. 1958;12(5):1693.

60. Scheffler K, Lehnhardt S. Principles and applications of balanced SSFP techniques. Eur Radiol. 2003 Nov;13(11):2409-18.

61. Scheffler K. A pictorial description of steady-states in rapid magnetic resonance imaging. Concepts Magn Reson. 1999;11(5):291-304.

62. Caravan P. Strategies for increasing the sensitivity of gadolinium based MRI contrast agents. Chem Soc Rev. 2006;35:512-23.

63. Silva AC, Bock NA. Manganese-enhanced MRI: An exceptional tool in translational neuroimaging. Schizophr Bull. 2008 Jul;34(4):595-604.

64. Chabanova E, Logager V, Moller JM, Dekker H, Barentsz J, Thomsen HS. Imaging liver metastases with a new oral manganese-based contrast agent. Acad Radiol. 2006 Jul;13(7):827-32.

65. Pautler RG. Biological applications of manganese-enhanced magnetic resonance imaging. Methods Mol Med. 2006;124:365-86.

66. Fiel RJ, Button TM, Gilani S, Mark EH, Musser DA, Henkelman RM, et al. Proton relaxation enhancement by manganese(III)TPPS4 in a model tumor system. Magn Reson Imaging. 1987;5(2):149-56.

67. Caravan P, Ellison JJ, McMurry TJ, Lauffer RB. Gadolinium(III) chelates as MRI contrast agents: Structure, dynamics, and applications. Chem Rev. 1999 Sep 8;99(9):2293-352.

68. Modo MMJJ. Molecular and cellular MR imaging. Hoboken: CRC Press; 2007.

69. Corot C, Robert P, Idee JM, Port M. Recent advances in iron oxide nanocrystal technology for medical imaging. Adv Drug Deliv Rev. 2006 Dec 1;58(14):1471-504.

70. Wang YX, Hussain SM, Krestin GP. Superparamagnetic iron oxide contrast agents: Physicochemical characteristics and applications in MR imaging. Eur Radiol. 2001;11(11):2319-31.

71. Shapiro EM, Skrtic S, Koretsky AP. Sizing it up: Cellular MRI using micron-sized iron oxide particles. Magn Reson Med. 2005 Feb;53(2):329-38.

72. Damadian R. Tumor detection by nuclear magnetic resonance. Science. 1971 Mar 19;171(976):1151-3.

73. Wallis F, Gilbert FJ. Magnetic resonance imaging in oncology: An overview. J R Coll Surg Edinb. 1999 Apr;44(2):117-25.

74. Wippold FJ, 2nd. Head and neck imaging: The role of CT and MRI. J Magn Reson Imaging. 2007 Mar;25(3):453-65.

75. Saslow D, Boetes C, Burke W, Harms S, Leach MO, Lehman CD, et al. American cancer society guidelines for breast screening with MRI as an adjunct to mammography. CA Cancer J Clin. 2007 Mar-Apr;57(2):75-89.

76. Gauvain KM, Garbow JR, Song SK, Hirbe AC, Weilbaecher K. MRI detection of early bone metastases in b16 mouse melanoma models. Clin Exp Metastasis. 2005;22(5):403-11.

77. Oliva MR, Saini S. Liver cancer imaging: Role of CT, MRI, US and PET. Cancer Imaging. 2004 Apr 2;4 Spec No A:S42-6.

78. Harisinghani MG, Hahn PF. Computed tomography and magnetic resonance imaging evaluation of liver cancer. Gastroenterol Clin North Am. 2002 Sep;31(3):759,76, vi.

79. Li W, Nissenbaum MA, Stehling MK, Goldmann A, Edelman RR. Differentiation between hemangiomas and cysts of the liver with nonenhanced MR imaging: Efficacy of T2 values at 1.5 T. J Magn Reson Imaging. 1993 Sep-Oct;3(5):800-2.

80. Weinmann H, Ebert W, Misselwitz B, Schmitt-Willich H. Tissue-specific MR contrast agents. Eur J Radiol. 2003 April, 2003;46(1):33-44.

81. Anzai Y. Superparamagnetic iron oxide nanoparticles: Nodal metastases and beyond. Top Magn Reson Imaging. 2004 Apr;15(2):103-11.

82. Weissleder R, Elizondo G, Josephson L, Compton CC, Fretz CJ, Stark DD, et al. Experimental lymph node metastases: Enhanced detection with MR lymphography. Radiology. 1989 Jun;171(3):835-9.

83. Bulte JW, Kraitchman DL. Iron oxide MR contrast agents for molecular and cellular imaging. NMR Biomed. 2004 Nov;17(7):484-99.

84. Arbab AS, Yocum GT, Rad AM, Khakoo AY, Fellowes V, Read EJ, et al. Labeling of cells with ferumoxides-protamine sulfate complexes does not inhibit function or differentiation capacity of hematopoietic or mesenchymal stem cells. NMR Biomed. 2005 Dec;18(8):553-9.

85. Crich SG, Biancone L, Cantaluppi V, Duo D, Esposito G, Russo S, et al. Improved route for the visualization of stem cells labeled with a gd-/Eu-chelate as dual (MRI and fluorescence) agent. Magn Reson Med. 2004 May;51(5):938-44.

86. Jirak D, Kriz J, Herynek V, Andersson B, Girman P, Burian M, et al. MRI of transplanted pancreatic islets. Magn Reson Med. 2004 Dec;52(6):1228-33.

87. Heyn C, Ronald JA, Ramadan SS, Snir JA, Barry AM, MacKenzie LT, et al. In-vivo MRI of cancer cell fate at the single-cell level in a mouse model of breast cancer metastasis to the brain. Magn Reson Med. 2006 Nov;56(5):1001-10.

88. Bernas LM, Foster PJ, Rutt BK. Magnetic resonance imaging of in vitro glioma cell invasion. J Neurosurg. 2007 Feb;106(2):306-13.

89. Dunn EA, Weaver LC, Dekaban GA, Foster PJ. Cellular imaging of inflammation after experimental spinal cord injury. Mol Imaging. 2005 Jan-Mar;4(1):53-62.

90. Oweida AJ, Dunn EA, Foster PJ. Cellular imaging at 1.5 T: Detecting cells in neuroinflammation using active labeling with superparamagnetic iron oxide. Mol Imaging. 2004 Apr;3(2):85-95.

91. Dardzinski BJ, Schmithorst VJ, Holland SK, Boivin GP, Imagawa T, Watanabe S, et al. MR imaging of murine arthritis using ultrasmall superparamagnetic iron oxide particles. Magn Reson Imaging. 2001 Nov;19(9):1209-16.

92. de Vries IJ, Lesterhuis WJ, Barentsz JO, Verdijk P, van Krieken JH, Boerman OC, et al. Magnetic resonance tracking of dendritic cells in melanoma patients for monitoring of cellular therapy. Nat Biotechnol. 2005 Nov;23(11):1407-13.

93. Cabella C, Crich SG, Corpillo D, Barge A, Ghirelli C, Bruno E, et al. Cellular labeling with gd(III) chelates: Only high thermodynamic stabilities prevent the cells acting as 'sponges' of Gd3+ ions. Contrast Media Mol Imaging. 2006 Jan;1(1):23-9.

94. Weissleder R, Elizondo G, Wittenberg J, Lee AS, Josephson L, Brady TJ. Ultrasmall superparamagnetic iron oxide: An intravenous contrast agent for assessing lymph nodes with MR imaging. Radiology. 1990 May;175(2):494-8.

95. Harada T, Tanigawa N, Matsuki M, Nohara T, Narabayashi I. Evaluation of lymph node metastases of breast cancer using ultrasmall superparamagnetic iron oxide-enhanced magnetic resonance imaging. Eur J Radiol. 2007 Sep;63(3):401-7.

96. Schroeter M, Jander S, Huitinga I, Witte OW, Stoll G. Phagocytic response in photochemically induced infarction of rat cerebral cortex. The role of resident microglia. Stroke. 1997 Feb;28(2):382-6.

97. Zhang Y, Dodd SJ, Hendrich KS, Williams M, Ho C. Magnetic resonance imaging detection of rat renal transplant rejection by monitoring macrophage infiltration. Kidney Int. 2000 Sep;58(3):1300-10.

98. Rocha PN, Plumb TJ, Crowley SD, Coffman TM. Effector mechanisms in transplant rejection. Immunol Rev. 2003 Dec;196:51-64.

99. Frank JA, Miller BR, Arbab AS, Zywicke HA, Jordan EK, Lewis BK, et al. Clinically applicable labeling of mammalian and stem cells by combining superparamagnetic iron oxides and transfection agents. Radiology. 2003 Aug;228(2):480-7.

100. Suzuki Y, Zhang S, Kundu P, Yeung AC, Robbins RC, Yang PC. In vitro comparison of the biological effects of three transfection methods for magnetically labeling mouse embryonic stem cells with ferumoxides. Magn Reson Med. 2007 Jun;57(6):1173-9.

101. Josephson L, Tung CH, Moore A, Weissleder R. High-efficiency intracellular magnetic labeling with novel superparamagnetic-tat peptide conjugates. Bioconjug Chem. 1999 Mar-Apr;10(2):186-91.

102. Frank JA, Anderson SA, Kalsih H, Jordan EK, Lewis BK, Yocum GT, et al. Methods for magnetically labeling stem and other cells for detection by in-vivo magnetic resonance imaging. Cytotherapy. 2004;6(6):621-5.

103. Hinds KA, Hill JM, Shapiro EM, Laukkanen MO, Silva AC, Combs CA, et al. Highly efficient endosomal labeling of progenitor and stem cells with large magnetic particles allows magnetic resonance imaging of single cells. Blood. 2003 Aug 1;102(3):867-72.

104. Shapiro EM, Skrtic S, Sharer K, Hill JM, Dunbar CE, Koretsky AP. MRI detection of single particles for cellular imaging. Proc Natl Acad Sci U S A. 2004 Jul 27;101(30):10901-6.

105. Geninatti Crich S, Cabella C, Barge A, Belfiore S, Ghirelli C, Lattuada L, et al. In vitro and in-vivo magnetic resonance detection of tumor cells by targeting glutamine transporters with gd-based probes. J Med Chem. 2006 Aug 10;49(16):4926-36.

106. Sun C, Sze R, Zhang M. Folic acid-PEG conjugated superparamagnetic nanoparticles for targeted cellular uptake and detection by MRI. J Biomed Mater Res A. 2006 Sep 1;78(3):550-7.

107. Baio G, Fabbi M, de Totero D, Ferrini S, Cilli M, Derchi LE, et al. Magnetic resonance imaging at 1.5 T with immunospecific contrast agent in vitro and in-vivo in a xenotransplant model. MAGMA. 2006 Dec;19(6):313-20.

108. Zurkiya O, Chan AWS, Hu X. MagA is sufficient for producing magnetic nanoparticles in mammalian cells, making it an MRI reporter. Magn Reson Med. 2008 June 2008;59(6):1225-31.

109. Cohen B, Dafni H, Meir G, Harmelin A, Neeman M. Ferritin as an endogenous MRI reporter for noninvasive imaging of gene expression in C6 glioma tumors. Neoplasia. 2005 Feb;7(2):109-17.

110. Misselwitz B. MR contrast agents in lymph node imaging. Eur J Radiol. 2006 Jun;58(3):375-82.

111. Kobayashi H, Kawamoto S, Sakai Y, Choyke PL, Star RA, Brechbiel MW, et al. Lymphatic drainage imaging of breast cancer in mice by micro-magnetic resonance lymphangiography using a nano-size paramagnetic contrast agent. J Natl Cancer Inst. 2004 May 5;96(9):703-8.

112. Harika L, Weissleder R, Poss K, Papisov MI. Macromolecular intravenous contrast agent for MR lymphography: Characterization and efficacy studies. Radiology. 1996 Feb;198(2):365-70.

Chapter 2 : Comparison of injection sites

2.1   Introduction

The use of relevant and reproducible animal models is of utmost importance in the study of cancer metastasis. Models for metastasis are especially challenging to design given the erratic behaviour of cancer cells in general. To effectively study metastasis, all the stages of the disease must be represented; formation of a primary tumor, dissemination of metastatic cells from the primary tumor, invasion into the lymphatics or circulatory system, and tumor development at the secondary site. The model must also be stable and reproducible.

There are three types of animal models used in cancer research: chemically induced cancer, genetically engineered mice and cancer cell transplantation models. Chemically induced models of cancer involve the repeated application of a carcinogen (1-3). Melanoma can be induced with an application of 7,12-dimethylbanz(a)anthracene (DMBA) and weekly application of croton oil, a known tumor promoter. With this method tumors develop 16 weeks after the application of DMBA (3). Chemically induced models best represent the natural course of tumor progression in a human. Tumors and metastasis both occur spontaneously (4). The difficulty with using chemically induced models is that the majority of these models do not metastasize (at least in mice), or metastasize after a very long latency period (5).

Genetically engineered mouse models are useful in determining genetic heterogeneity of tumor phenotypes and are useful in studies of cancer prevention. Studies using p53

knockout mice have shown that calorie restriction reduces cell proliferation and suppresses the progression of prenoplastic cells (6). Genetically engineered models, though faster than chemically induced models, take months to develop metastasis. It is also difficult to stage or detect metastatic disease in these animals because of the variability in tumor dissemination (5).

Transplantation models can be divided into two subcategories: experimental and spontaneous. Experimental transplant metastasis models involve the injection of cancer cells directly into the circulatory system. Disease progression occurs quickly in these models. The disadvantage of experimental metastasis models is that they bypass cell dissemination from the primary tumor that could have distinct characteristics that are associated with successful metastasis. Spontaneous transplant models implant cells subcutaneously, or at the orthotopic site, which is the site of natural occurrence for the specific cancer (5). These models have produced tumors that more closely resemble human cancers in terms of tumor histology, gene expression and metastatic biology (7). Primary tumors form quickly at the implant site in these models and investigations of the metastatic cascade from formation of tumor to development of secondary tumors is possible. Transplantation models allow the researcher to control the number and type of cell used. These models are useful for imaging studies because the cells can be modified such that in-vivo detection is possible.

In this study we compare two spontaneous transplant models of metastatic melanoma in the mouse: the direct implantation of B16F10 cells into the inguinal lymph node and the implantation of B16F10 cells subcutaneously into the flank. The main objective was to determine whether the direct intranodal injection of cells would produce a robust and reliable model for imaging metastasis of cancer cells in the lymph nodes.

2.2 Methods

2.2.1 Cell labeling

Mouse melanoma cells (B16F10) were maintained in Dulbecco's modified Eagle's medium (DMEM) containing 10% Fetal Bovine Serum (FBS) at 37° C and 5% CO_2. Cells were plated in 6 well plates at 2.5×10^5 cells and 2 ml of media in each well. After 24 hours the media was replaced with new media and 9.41×10^6 micron-size iron-oxide particles (MPIO, 0.9 µm diameter, Bangs Laboratory, Fishers, IN, USA) were added to each well. The cells were incubated with MPIO for 24 hours. Cells were washed 4 times with Hank's Buffered Salt Solution to remove any unincorporated iron. Cell viability was tested with the trypan blue exclusion and plating efficiency assays. After cell harvesting a subset of cells were diluted for injection and the remaining cells were kept in sterile conditions for plating efficiency assays. 100 cells were plated on a petri dish with 10 ml of media. Cells were counted using a haemocytometer. The dish was monitored starting 7 days post plating for the appearance of cell colonies. The development of colonies occurred between 7-10 post plating. Once cell colonies were visible the media was removed from the dish and the colonies were fixed with 10% formalin for 10 minutes. After the removal of the formalin 0.5% cresyl violet blue was added to the dish for 5 minutes before the plate was rinsed with double distilled water. The number of colonies were then counted. Plating efficiency was found by the number of colonies counted divided by the number of cells plated.

2.2.2 Animal Models

C57Bl/6 mice (female, 6 weeks old, Charles River Laboratories, Wilmington, MA, USA) were anesthetized with the gas anesthetic isoflurane (1.5% in 100% oxygen). Two

injection sites were used: a subcutaneous injection into the right flank and an injection of cells directly into the right inguinal lymph node. Injections in the right flanks were performed with a 30 gauge needle. For the intranodal injections a small superficial incision was made to the abdomen right of the midline exposing the inguinal lymph node. The cells were then implanted directly into the inguinal node using a specially designed experimental needle (30 gauge, Becton Dickinson Technologies). Animals were injected with 10,000 B16F10 cells in 5 μl PBS. The wound was then closed with tissue glue (Vetbond, 3M company, St. Paul, MN). Animals were sacrificed 28 days post injection or earlier depending on the health of the animal. Four groups were used: group 1 received an injection of unlabeled cells subcutaneously in the flank (n=12), group 2 received an injection of labeled cells subcutaneously in the flank (n=18), group 3 received an injection of unlabeled cells in the node (n=6), and group 4 received an injection of labeled cells in the node (n=6).

2.2.3 Post-Mortem Analysis

All animals underwent a post-mortem examination by dissection. Melanoma cells and tumors were easily visualized by the brown pigmentation produced by melanin. Nodes were classified as follows: "Speckled" which characterized sparse areas of discolouration on the surface of the node that indicated the presence of cells in the node but had not yet developed into a tumor mass, "micro" which indicated dot-like tumor mass(es) on the surface of the lymph node, "small" describes tumor foci that was <50% of the total nodal surface and "large" describes tumor foci that had taken over the entire node or is ≥50% of the total nodal surface. Growths at the site of implantation were referred to as "tumors". The right inguinal node/tumor, the right axillary nodes and all other tissues with tumors or

suspected of having melanoma cells within the tissue were removed and processed for histology.

2.2.4 Statistical Analysis

The student t-test was performed to compare the number of nodes with metastasis between labeled and unlabeled cells in the two implantation groups using Microsoft Excel 2002 (Microsoft, Redmond, WA, USA).

2.2.5 Iron Measurement

Intracellular iron content was measured using both a susceptometry measurement and inductively coupled plasma mass spectrometry (ICP-MS). For susceptometry measurements cells were spun down to a concentration of 2×10^6 cells/ml. Cells were resuspended in 1 ml PBS. 8% gelatin was made and filtered. 500 µl of cells was added to 500 µl of 8% gelatin and injected into a NMR tube. The tube was then capped and placed on ice until the gelatin solidified and then stored at 4°C until ready for measurement. Iron content measurement was made using the Reilly-McConnell-Meisenheimer susceptometry technique modified for multi-echo imaging (8).

2.3   Results

2.3.1   Cell Labeling

Plating efficiency tests were only successfully conducted for cells used for groups 1 and 2, where the efficiencies were 92% and 100% for unlabeled and labeled cells. The average amount of iron per cell was 68 pg of iron/cell.

2.3.2   Post-mortem analysis

In group 1, 3 animals had tumors that were palpable by day 11, 3 by day 14, 4 by day 20 and 1 by day 25. One animal had a tumor that was not palpable and could only be seen upon dissection. All 12 animals in group 1 developed tumors. Tumor weights ranged from < 0.1-7.84 g.

In group 2, 1 animal had a tumor that was palpable by day 13, 3 by day 14, 1 by day 17, 6 by day 20, and 2 by day 27. One animal had a tumor that was not palpable. Tumors developed in 14/18 animals, with tumor weights ranging between 0.13-4.74 g. A total of 8 nodes, or 27% of the animals with thigh injections (both labeled and unlabeled), had metastases upon gross dissection. Half of the metastases were in the medial iliac node (in the abdomen of the mouse by the bladder). The other nodes affected by metastases were the brachial, inguinal and axillary nodes. The student t-test revealed that there was no significant difference between the number of nodes with metastases in the labeled and unlabeled groups (p-value=0.69).

In group 3 all 6 animals developed tumors, with tumor weights ranging between 0.98 -7.38 g. Group 3 had 3 animals that had palpable tumors by day 11 and 3 by day 14. Group

4 had 4 animals with palpable tumors by day 14 and one palpable tumor by day 28. 5/6 animals developed tumors, with tumor weights ranging between 0.23-4.61 g. A total of 4 nodes, or 33% of the animals with an intranodal (both labeled and unlabeled) injection had metastases in the distant node. All metastases were found in the axillary node (in the armpit of the mouse). A p-value of 0.18 was found and therefore there was not a significant difference between the number of node with metastases in the labeled and unlabeled groups.

A summary the number of tumors formed at the implant site and the total number of metastases in each group of animals is found in Table 2.1.

Group	Sample Size	# of tumors at implant site	# nodes with metastases
Unlabeled Flank	12	12	4
Labeled Flank	18	14	4
Unlabeled Node	6	6	3
Labeled Node	6	5	1

Table 2.1: Summary of Tumor Formation and Metastases

There was no significant difference between the number of nodes with metastases between the subcutaneous implantation of cells in the flank and an implantation of cells in the node (p=0.37).

Each distant node with metastases was graded post-mortem. The grade of each metastatic node from each injection site (both labeled and unlabeled) is summarized in Table 2.2.

Injection Site / Grade	Subcutaneously in flank	Directly in inguinal node
Speckled	2	0
Micrometastases	4	1
Small metastases	1	2
Large metastases	1	1

Table 2.2: Grading of Nodes with Metastasis

2.4 Discussion

Metastasis to the lymphatics is a poorly understood process. Development of models of spontaneous metastasis are even more challenging since the cells must be aggressive enough to metastasize but not grow too quickly to warrant a premature end-point of the experiment. Numerous models of lymphatic metastasis have been developed, many utilizing an orthotopic site of implantation. Orthotopic transplantation models are advantageous since they result in a more accurate representation of natural tumor progression. Human cervical carcinoma implanted into the uterus in mice (9, 10), human hepatocellular carcinoma implanted in the livers of mice (10) and a variant of human breast adenocarcinoma injected in the mammary fat pad (12) have all been shown to aggressively metastasize to the regional lymph nodes. The Lewis lung carcinoma is a lung cancer that occurred spontaneously in a C57Bl/6 mouse. This cell line has been used as a model for metastatic cancer in the lymph nodes with an injection of cells in matrigel directly in the lungs of C57Bl/6 mice (13). The disadvantages of the use of orthotopic models of cancer are that they are technically demanding and often require the use of immune-compromised mice.

The B16F10 melanoma cell line allows experimentation using normal mice with fully functioning immune systems. This cell line has been used to develop various models of lymphatic metastasis. Ishibahsi et al. found that after an injection of 10,000 B16F10 cells into the retroperitoneal space in mice (n=10) only 2 intra-abdominal nodes developed metastasis (14). Other B16F10 models involve subcutaneous injections into the footpad (15) and tail (16). These models are minimally invasive and are relatively simple to perform.

Like the previously mentioned models using B16F10, the two implantation sites tested here were also minimally invasive, with the subcutaneous model requiring no

49

incisions and the intranodal model requiring a small superficial cut. The subcutaneous implantation model is a more realistic model then that of the intranodal model. The subcutaneous site is closer to the orthotopic site of melanoma. In the subcutaneous model the cells have to disseminate from the tumor at the implant site to the lymphatics, whereas in the intranodal model the cells are implanted directly into the lymph node.

There was a wide range of tumor weights at the implant site in both models. A high occurrence of cancer growth at the implant site was found in both models with palpable tumors occurring by day 11 post-injection. Though the percentage of animals with nodal metastasis was larger in the intranodal model than the flank model, there was no significant difference between the two groups. However, the intranodal cell implant did result in metastases only in the axillary node, whereas the subcutaneous cell implant resulted in metastases in several different lymph nodes. The variability in the sites of metastasis in the subcutaneous model could be attributed to the abundance of blood and lymphatic vessels located within the subcutis (hypodermis) layer of the skin where the cells were implanted. Both types of vessels are present in the lymph nodes. The ample amount of vessels gives the cells a variety of different pathways in which they could migrate leading to variations in the nodes with disease between animals with a flank implantation. The predictability of the intranodal model is advantageous for imaging studies because the location of metastatic development is known.

In the intranodal model half the metastases were graded as "small" while the majority of metastases in the subcutaneous model were considered "micro". The development of larger metastatic tumors with the intranodal model can be both a disadvantage and an advantage. The MPIO label could dilute more quickly in rapidly dividing cells but the

detection of metastases is easier with larger tumors. The flank injections resulted in tumor growth within the muscle, which made analysis of the tumor itself very difficult since the removal of the entire leg was often necessary to keep the tumor at the implant site intact. The subcutaneous injection in the flank also resulted in the outward growth of the tissue, which decreased mobility and increased the width of the animals significantly. The tumors from the node injection tend to grow inward causing less of a size increase in the animals. The RF coils used to image the animals are of a fixed diameter and placement of the animal in the coil is difficult with the expansion of leg size in the subcutaneous model. Several animals from the subcutaneous implantation group also had tumors that ulcerated and none in the intranodal model did. In accordance to the animal care protocol the occurrence of either of these events requires that the animal be sacrificed. This resulted in an early endpoint for mice receiving the subcutaneous cell injections.

2.5 Conclusion

The MPIO agent did not affect the growth of B16F10 cells or the metastatic ability. The intranodal model resulted in a higher percentage of metastasis to the distant lymph nodes (though not significantly different), an inward growth of the tumor and a consistent location for metastases in the axillary node when compared to the subcutaneous implantation in the flank. Overall, the intranodal model of metastasis was determined to be the better model than the subcutaneous implantation of cells in the flank for imaging studies involving metastasis to the lymph nodes.

2.6 References

1. Wang Y, Zhang Z, Yan Y, Lemon WJ, LaRegina M, Morrison C, et al. A chemically induced model for squamous cell carcinoma of the lung in mice: Histopathology and strain susceptibility. Cancer Res. 2004 Mar 1;64(5):1647-54.

2. D'Agostini F, Balansky RM, Bennicelli C, Lubet RA, Kelloff GJ, De Flora S. Pilot studies evaluating the lung tumor yield in cigarette smoke-exposed mice. Int J Oncol. 2001 Mar;18(3):607-15.

3. Berkelhammer J, Oxenhandler RW, Hook RR,Jr, Hennessy JM. Development of a new melanoma model in C57BL/6 mice. Cancer Res. 1982 Aug;42(8):3157-63.

4. Teicher BA. Tumor models in cancer research. Totowa, N.J.: Humana Press; 2002.

5. Khanna C, Hunter K. Modeling metastasis in-vivo. Carcinogenesis. 2005 Mar;26(3):513-23.

6. Hursting SD, Perkins SN, Phang JM. Calorie restriction delays spontaneous tumorigenesis in p53-knockout transgenic mice. Proc Natl Acad Sci U S A. 1994 Jul 19;91(15):7036-40.

7. Poste G, Doll J, Hart IR, Fidler IJ. In vitro selection of murine B16 melanoma variants with enhanced tissue-invasive properties. Cancer Res. 1980 May;40(5):1636-44.

8. Bown CV, Zhang X, Saab G, Gareau PJ, Rutt BK. Application of the static dephasing regime theory to superparamagnetic iron-oxide loaded cells. Magn Reson Med. 2002 Jul;48(1):52-61.

9. Cairns RA, Hill RP. Acute hypoxia enhances spontaneous lymph node metastasis in an orthotopic murine model of human cervical carcinoma. Cancer Res. 2004 Mar 15;64(6):2054-61.

10. Qiu C, Wu H, He H, Qiu W. A cervical lymph node metastatic model of human tongue carcinoma: Serial and orthotopic transplantation of histologically intact patient specimens in nude mice. J Oral Maxillofac Surg. 2003 Jun;61(6):696-700.

11. Sun FX, Tang ZY, Lui KD, Ye SL, Xue Q, Gao DM, et al. Establishment of a metastatic model of human hepatocellular carcinoma in nude mice via orthotopic implantation of histologically intact tissues. Int J Cancer. 1996 Apr 10;66(2):239-43.

12. Vantyghem SA, Allan AL, Postenka CO, Al-Katib W, Keeney M, Tuck AB, et al. A new model for lymphatic metastasis: Development of a variant of the MDA-MB-468 human breast cancer cell line that aggressively metastasizes to lymph nodes. Clin Exp Metastasis. 2005;22(4):351-61.

13. Doki Y, Murakami K, Yamaura T, Sugiyama S, Misaki T, Saiki I. Mediastinal lymph node metastasis model by orthotopic intrapulmonary implantation of Lewis lung carcinoma cells in mice. Br J Cancer. 1999 Mar;79(7-8):1121-6.

14. Ishibashi S, Sonoda K, Fujii K, Ishikawa K, Shiraishi N, Kitano S. A convenient murine model for the study of intra-abdominal lymph node metastasis. Oncol Rep. 2004 Jul;12(1):115-8.

15. Nathanson SD, Haas GP, Mead MJ, Lee, M. Spontaneous regional lymph node metastases of three variants of the B16 melanoma: Relationship to primary tumor size and pulmonary metastases. J Surg Oncol. 1986;33(1):41-5.

16. Shrayer DP, Bogaars H, Wolf SF, Hearing VJ, Wanebo HJ. A new mouse model of experimental melanoma for vaccine and lymphokine therapy. Int J Oncol. 1998 Aug;13(2):361-74.

Chapter 3 : MRI Cell Tracking of Metastatic Melanoma in Mouse Lymph Nodes

3.1 Introduction

The role of the lymphatics as a mode of tumor cell transport has been known for some time, and remains of critical importance since a majority of cancer deaths result from metastatic dissemination away from the primary tumor (1, 2). The contributions of the blood vascular system to metastasis have been intently studied (3-7). Influenced by this work, recent evidence points to a similar complexity for lymph mediated metastasis comprising a series of sequential, interrelated steps (8).

The presence, location, and size of cancer cells within nodes and the number of involved nodes already form the basis of staging for a variety of solid tumors and the prognosis for patients with lymphoid micrometastases (0.2-2.0 mm) is more favorable than for those with macrometastases (9, 10). The clinical significance of discovering single cancer cells or micrometastases in lymph nodes is really not clear. Van Akkooi et al. reported that sentinel lymph nodes with micrometastases less than 0.1 mm in diameter could be considered negative for disease and that complete lymph node dissection would not be beneficial for these patients (11). They also found no correlation between the location or thickness of the metastases and non-sentinel lymph node positivity, disease-free survival, or overall survival (11). In contrast, Li et al. showed that there was disease recurrence in the same nodal basin in patients with metastases in the sentinel lymph nodes as small as 0.025 mm (12). Moreover, others have found staging parameters other than the diameter of metastatic tumors in the sentinel lymph node to be good predictors of disease in other nodes

(13, 14). These discrepancies may be related to differences in tissue sectioning and staining protocols and intraobserver variability.

All current cancer cell detection methods rely on tissue dissection with biopsy and histology remaining the gold standard for detecting metastatic spread to the lymph nodes. These methods are invasive, cross-sectional, labor intensive and provide only a "snapshot" of the overall processes. Clearly, studies of lymphatic cancer metastasis would benefit from a non-invasive method of nodal interrogation.

Magnetic resonance imaging (MRI) is a strong candidate imaging modality for the detection of lymphatic metastasis because it is noninvasive, without ionizing radiation, has high spatial resolution and high tissue contrast. Unlike histological analyses, MRI can provide a more dynamic view of disease in-vivo. Standard lymphatic anatomical MR imaging is limited to the detection of nodes that are enlarged and/or irregular (15). This is a pitfall, since micrometastases can often be found in normal sized and shaped nodes. Also, things other than malignancy such as a bacterial infection may cause enlarged nodes. Both iron based and gadolinium (Gad) based contrast agents are currently undergoing testing to increase the utility of this imaging modality for lymph diagnoses (16-18).

A number of different iron based magnetic nanoparticles (MNP) are available for research (19). MNP are administered intravenously and slowly accumulate in the lymph node macrophages (20). MR images are typically acquired 24 hours after the administration of MNP. The presence of this magnetic label in cells causes a distortion in the magnetic field and leads to signal hypo-intensities (negative contrast) in images sensitive to this change (T2- or T2*-weighted images) (21). The region of signal loss is the image typically much

larger than the actual area occupied by the cells, an effect known as the 'blooming' artifact (22).

In malignant nodes, the normal tissue appears with low signal and the metastatic tissue appears unchanged. Several studies have demonstrated enhanced nodal MR imaging after IV administration of MNP, and some iron agents are in clinical trials (23). However, false negatives may result when there is enough normal tissue taking up iron to cause the whole node to appear black because of blooming, effectively hiding metastatic tissue. In addition, reactive nodes containing primarily lymphocytes, which do not take up iron, may result in false positives (15). Gadolinium (Gad) based agents have been used to visualize normal lymph nodes and nodal tumors in rabbits and mice (24, 25). With Gad based agents, normal node tissue appears bright in the images, whereas metastatic tissue remains unchanged. Neither MNP nor Gad based agents provide direct visualization of cancer cells in nodes when administered IV; both methods work by changing the signal intensity of normal nodal tissue.

Cellular MRI is a newly emerging field of imaging that combines ultra-high resolution MRI with the use of sensitive cell labeling agents for the direct imaging of cells (26, 27). The majority of research in this area has utilized MNP because of their greater sensitivity compared to Gad-based agents. In experimental cellular MRI, cells are typically loaded with MNP prior to their injection or implantation. The resulting signal hypo-intensities can be tracked in-vivo providing information about the presence, location and migration of the iron-labeled cells. In 2006, we showed that even single iron-labeled cells can be visualized in-vivo using MRI (28).

Recently we showed that as few as 100 iron-labeled melanoma cells could be visualized after their direct implantation into the inguinal lymph node in mice (29). In Chapter 2 of this thesis, that intranodal model of melanoma metastasis was shown to be a better model than the subcutaneous model, which is a more traditional model of melanoma metastasis, for imaging purposes. The combination of inward growth of the tumor at the implant site and the known location of distant metastases made this model more suitable for imaging experiments. Here, we extend our previous work with this model and demonstrate the ability to track the movement of iron-labeled melanoma cells from a primary implant site to a distant lymph node. In this paper we demonstrate, for the first time, that cellular MRI can be used to detect metastatic melanoma cells present in the draining lymph node, and to track the growth of these cells into a metastatic tumor.

3.2   Methods

3.2.1   Cell Culture and Labeling

Mouse melanoma cells (B16F10) were maintained in Dulbecco's modified Eagle's medium (DMEM) containing 10% Fetal Bovine Serum (FBS) at 37° C and 5% CO_2. Cells were plated in 6 well plates at 2.5×10^5 cells with 2 ml of media in each well. After 24 hours the media was replaced with new media and 9.41×10^6 micron-size iron-oxide particles (MPIO, 0.9 μm diameter, Bangs Laboratory, Fishers, IN, USA) were added to each well. The cells were incubated with MPIO for 24 hours. Cells were washed 4 times with Hank's Buffered Salt Solution to remove any unincorporated iron. Cell viability was tested with the trypan blue exclusion and plating efficiency assays. After cell harvesting a subset of cells were diluted for injection and the remaining cells were kept in sterile conditions for plating

efficiency assays. 100 cells were plated on a petri dish with 10 ml of media. Cells were counted using a haemocytometer. The dish was monitored starting 7 days post plating for the appearance of cell colonies. The development of colonies occurred between 7-10 days post plating. Once cell colonies were visible the media was removed from the dish and the colonies were fixed with formalin for 10 minutes. After the removal of the formalin 0.5% cresyl violet blue was added to the dish for 5 minutes before the plate was rinsed with double distilled water. The colonies were then counted. Plating efficiency was defined as the number of colonies counted divided by the number of cells plated.

3.2.2 Animal Model

C57Bl/6 mice (female, 6 weeks old, Charles River Laboratories, Wilmington, MA, USA) were anesthetized with the gas anesthetic isoflurane (1.5% in 100% oxygen). A small superficial incision was made to the abdomen right of the midline exposing the inguinal lymph node. 10,000 B16F10 cells in 5 μl PBS were implanted directly into the inguinal node using a specially designed needle for (30 gauge, Becton Dickinson Technologies). The wound was then closed with tissue glue (Vetbond, 3M company, St. Paul, MN).

Group 1 consisted of thirty mice implanted with MPIO-labeled cells in the right inguinal node. Group 2 consisted of six mice implanted with unlabeled cells in the right inguinal node. Group 3 consisted of twelve mice implanted with MPIO-labeled cells in the right inguinal node and with unlabeled cells in the left inguinal node.

3.2.3   MRI

Imaging was performed on a 1.5T GE CV/1 whole body clinical MR scanner using a custom-built, insertable gradient coil (inner diameter=17.5 cm, maximum gradient strength=500 mT/m, and peak slew rate= 3000 mT/s) and a custom-built mouse body radiofrequency coil (inner diameter= 4 cm) [Figure 2.1]. Anesthesia was induced and maintained with isoflurane (1.5 % in 100% oxygen) delivered to the animals via a nose cone and scavenged by vacuum. Mice were kept warm during the scanning with the use of heated water pads. Images of the whole mouse body were acquired using the 3D fast imaging employing steady state acquisition (3D-FIESTA) pulse sequence. The imaging parameters were: repetition time = 9.2ms, echo time = 4.1ms, flip angle = 30°, 2 signal averages, spatial resolution = 200 μm^3 isotropic, scan time = 23 minutes. Twenty of the thirty mice from Group 1 were part of a longitudinal imaging experiment and were imaged five times after cell implantation, on days 0 or 1, 7, 14, 21 and 28 (in some cases day 28 images could not be acquired because tumors growth was too large). All twenty mice were sacrificed after the last imaging session (day 21 or 28). The remaining ten mice from Group 1 were part of a cross-sectional experiment with two mice scanned and then sacrificed at each time point, days 0, 7, 14, 21 and 28. Mice from Group 2 were part of a longitudinal experiment and were imaged on days 0, 7, 14, 21 and 28 post-implantation. Mice from Group 3 were part of a cross sectional experiment with two mice scanned and then sacrificed at each of days 0, 7 and 14 post cell implantation.
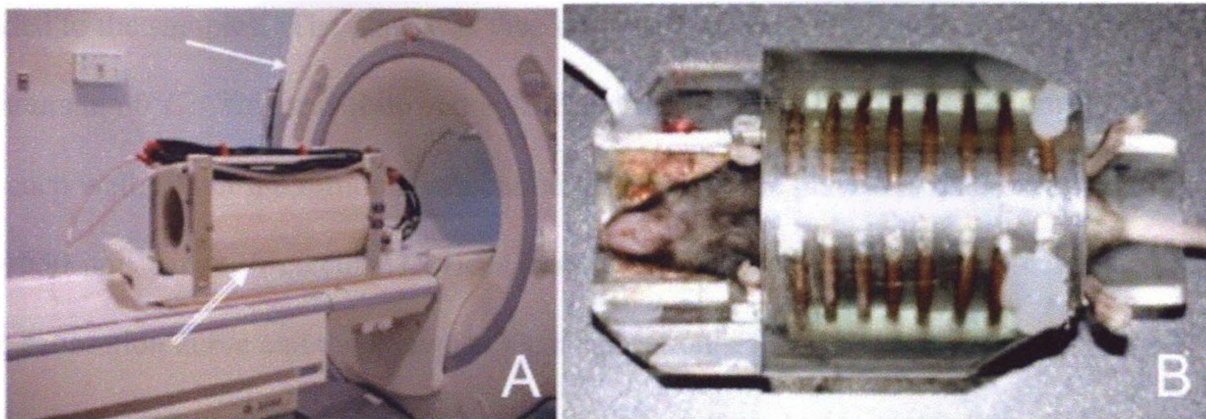
Figure 3.1: Customized Hardware for Cellular MRI.

(A) A specialized gradient insert coil (double lined arrow) utilized for our experiments. The gradient coil is placed directly in the bore of a 1.5T GE scanner (single arrow) making it capable of producing ultra-high resolution images in short scan times. (B) A custom-built solenoid RF coil, with an inner diameter of 4 cm, built specifically for whole body mouse image. A mouse nose cone sat on the end of the mouse bed to deliver gas anesthesia.

3.2.4   Image Analysis

All MRI images were assessed for regions of signal loss in the implanted node and in draining lymph nodes. Tumor and lymph node volumes were measured using an image data analysis package (OsiriX, GNU Open source license). The lymph node/tumor boundaries were outlined using the region of interest tool in OsiriX. Lymph node/tumor boundaries were manually segmented from the slice where the tissue of interest first appeared and each subsequent slice until the tissue of interest was no longer visible. The number of slices segmented per image sequence ranged from 25-220.

3.2.5   Measurements of Iron Content

Intracellular iron content was measured using a colorimetric assay. Three wells of a 96 well plate were each plated with 2.5×10^5 cells in 100 μl of HBSS. Samples with known concentrations of iron were also plated in triplicate to measure a calibration curve. The plate was then placed uncovered in an oven at 80°C overnight after which 100 μl of 5 M HCl was

added to the samples. The plate was then covered and placed back into the oven for another 5 hours at 60°C. This was followed by the addition of 100 µl of 5% potassium ferrocyanide to each well. After a 15 minute incubation in the dark, the plate was read on a spectrometer (λ=650 nm, Vmax, Molecular Devices, Sunnyvale, CA). Iron content was calculated using the calibration curve and the known cell concentration.

Iron content was measured for 10 axillary lymph nodes using inductively coupled plasma spectrometry (ICP-MS). 2 mice were sacrificed at each of the five time points post-implantation (days 1, 7, 14, 21 and 28) for a total of 10 animals. 5 mice were from Group 1, 2 mice were from Group 2, and 3 mice were from Group 3, where only the nodes from the side of the animal that received an implantation of unlabeled cells were used for ICP-MS measurements. The axillary nodes were surgically removed immediately after sacrifice and placed inside a 1.5 ml microcentrifuge tube (Eppendorf Canada, Mississauga, Canada). Samples were kept in a -20°C freezer until ICP-MS analysis was performed.

3.2.6   Post Mortem Analysis and Histology

All animals underwent a post-mortem examination by dissection. Melanoma cells and tumors were easily visualized by the brown pigmentation produced by melanin. Metastases on nodes were classified as follows: "speckled" which described nodes with sparse, discrete points of discolouration on the surface of the node, "micro" which indicated clusters of dot-like tumor mass(es) on the surface of the lymph node, "small" describes tumor foci that occupied less than 50% of the total nodal surface and "large" describes tumor foci that had taken over the entire node or occupied greater than 50% of the total nodal surface. Growths at the site of implantation were referred to as "tumors". The right inguinal

node/tumor, the right axillary nodes and all other tissues with tumors or suspected of having melanoma cells within the tissue were removed and processed for histology.

Tissues were embedded in paraffin and 8 μm thick tissue sections were cut from the block and placed on glass slides. Contiguous sections were stained with hematoxylin and eosin (H&E), to visualize cellular and general tissue structure and Perl's Prussian Blue (PPB), counterstained with eosin (to stain the cytoplasm) for iron staining. All slides were studied with a microscope (Eclipse E400, Nikon, Canada) and photographs of the slides were taken with a digital camera (Retiga, Q Imaging, Canada) and imaging processing software (ImagePro, Media Cybernetics, USA).

3.3   Results

3.3.1   B16F10 Cell Labeling

The mean iron loading per cell was measured to be 49.9±13.4 pg of Fe/cell. Plating efficiency tests showed that cell viability was 85±12% for labeled cells and 84±16% for unlabeled cells (data not shown). Trypan blue exclusion assay showed <5% cell death after harvesting.

3.3.2   In-Vivo Imaging

In 30/30 mice implanted with MPIO-labeled cells in the right inguinal node, signal loss was observed within the implanted node in images acquired on day 0 or 1 post-implantation. Figure 3.2 shows images of a sample mouse and the development of the tumor from MPIO-labeled cells. On day 1 (2A) a dense region of signal loss was typically visible within the inguinal lymph node, often large enough in size to mask the node itself. On day 7

(2B) images show a focal area of signal loss within the node and a visible increase in the node size suggesting that the development of a solid tumor mass has begun. On day 10 (2C) a further increase in size of the implanted node can be observed and the region of signal loss appears to be still focal but slightly dispersed in the expanding mass. On day 14 (2D) the areas of signal loss in the growing tumor become much more sparse and dispersed throughout the tumor. In images acquired on day 21(2E) a large nodal tumor is apparent with only small residual regions of signal loss observed.
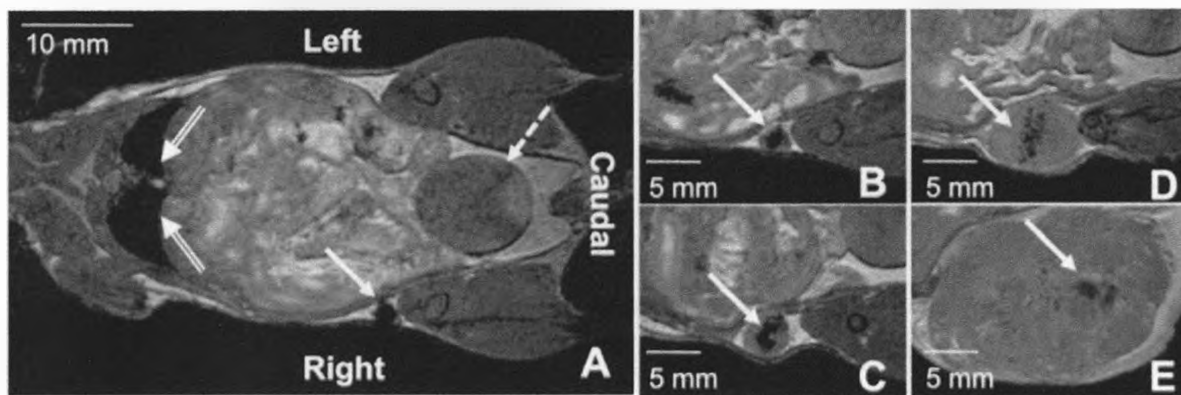
Figure 3.2: Tumor at Inguinal Node Implant Site

(A) A sample coronal FIESTA image slice of the mouse body at day 1 post-implantation. Anatomical landmarks including the lungs (double arrow) and bladder (dashed) are clearly visible. At the site of implantation a dense area of signal loss is visible (arrow). In (B-D) images are cropped and enlarged to highlight the inguinal node at days 7 (B), 10 (C), 14 (D) and 21 (E) post-implantation. With time, as a tumor develops at the site of implantation, the region of signal loss becomes dispersed.

In 21 of these 30 mice signal loss was also observed in the first draining lymph node, the axillary node. In 17 of these 21 animals the signal loss was observed in the first scan, in images acquired on day 0 or 1 post-implantation. Signal loss within these axillary nodes persisted until at least day 14. Sample images from one of these mice are shown in Figure 3.3. The hypointense area persisted until day 14 (3E). In images acquired on day 21 post-

implantation a tumor was observed at the axillary node (3F). The tumor at the axillary node

no longer contained a region of signal loss.

Figure 3.3: Signal Loss in Distant Node on Day 1 Post-Implantation

(A,B) Cropped coronal FIESTA image slices of the mouse body at day 21 post-implantation show the axillary node (box in A) and the implantation site (inguinal node, dashed arrow in B). In (C-G) images are cropped and enlarged to highlight the axillary node (arrows) at days 1 (C), 7 (D), 10 (E), 14 (F) and 21 (G) post-implantation. Signal loss appears in the axillary lymph node in images acquired on day 1 and persists until a metastatic tumor is visible in images acquired at day 21.

In 4 of the 21 mice a region of signal loss within the axillary node was not observed

in the first scan (as in the other 17 mice), but was detected in images acquired several days

post-implantation. Three mice showed hypointensity in the axillary node 21 days post-

implantation of cells and one mouse had hypointensity in the axillary node 7 days post-

implantation. Images of these animals are shown in Figures 3.4-3.7. Figure 3.4 shows an animal with signal loss observed 21 days post-implantation. At dissection a large metastasis in the axillary node was noted, corresponding to the MR images. Figures 3.5 and 3.6 shows the remaining two animals with signal loss in the axillary node 21 days post-implantation. Post-mortem analysis revealed that the node was "speckled" for the animal in Figure 3.5 and the animal in Figure 3.6 had to 2 small metastases in the axillary node. A large metastases was noted upon dissection for the animal in Figure 3.7 where signal loss was observed in the axillary node 7 days post-implantation of cells. For these 21 mice, observations noted at dissection included 7 axillary nodes which were speckled, 2 axillary nodes with micrometastases, 3 axillary nodes with small metastases, and 7 axillary nodes with large metastases. 2 axillary nodes did not have any evidence of disease upon gross dissection.

In five mice metastatic tumors, which were not detected as regions of signal loss by MRI, were discovered in the axillary node at dissection. In one animal, two small metastases in the axillary node were not noticed until the post-mortem examination. Two animals had large metastasis and two had speckled nodes at post-mortem.

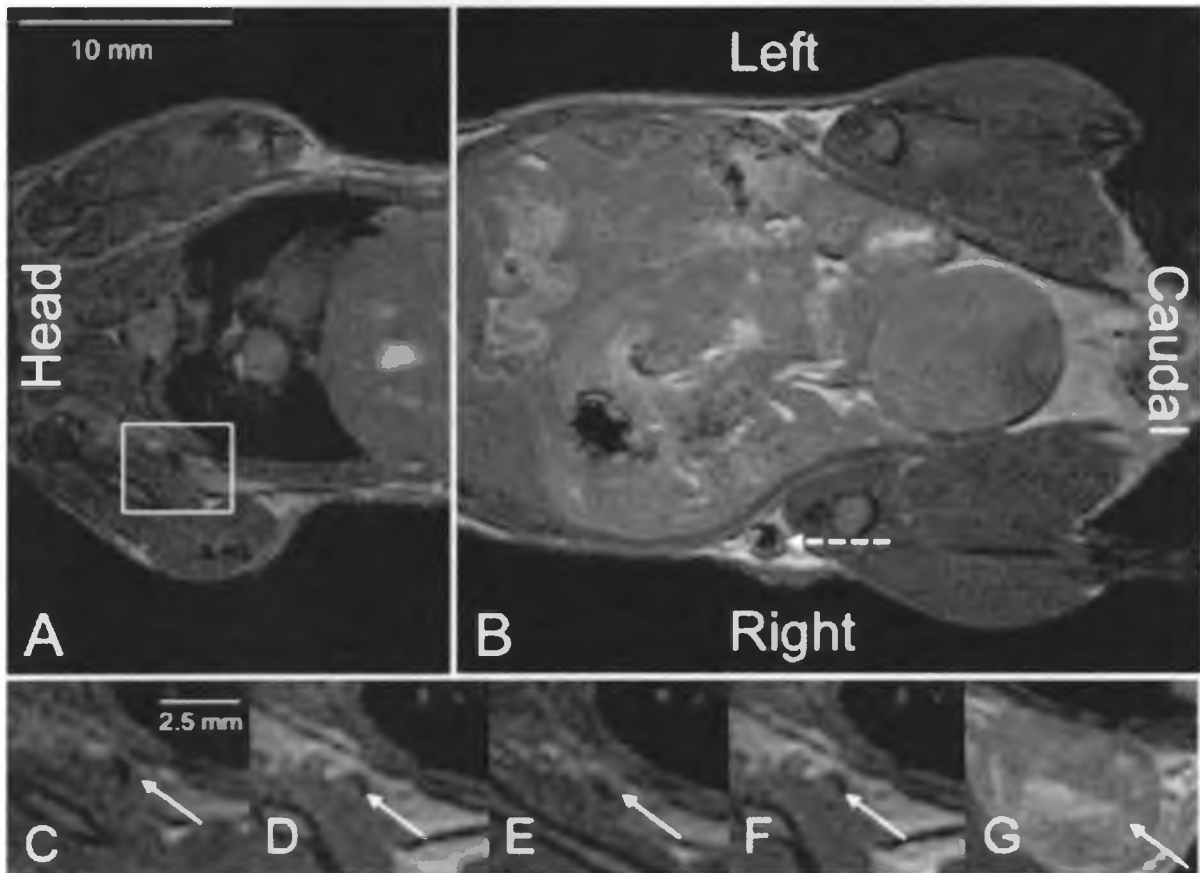***Figure 3.4: Appearance of Signal Loss Day 21 Post-Implantation***

(A,B) Cropped coronal FIESTA image slices of the mouse body at day 21 post-implantation show the axillary node (A) and a massive tumor at the site of implantation (B). In (C-F) images are cropped and enlarged to highlight the axillary node at days 0(C), 7 (D), 14 (E) and 21 (F) post-implantation. Signal loss appears in the axillary lymph node in images acquired on day 21.
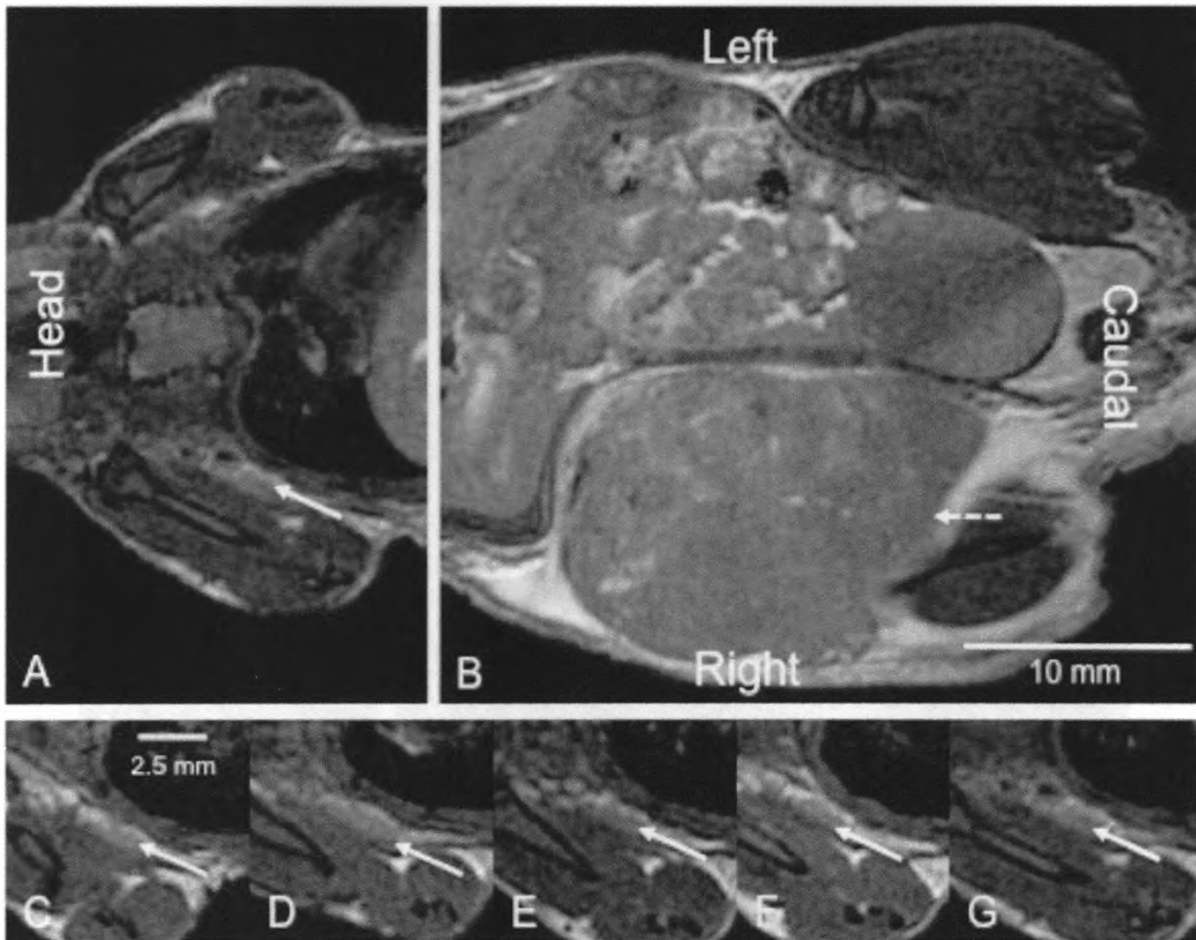
Figure 3.5: Appearance of Signal Loss Day 21 Post-Implantation Example 2

(A,B) Cropped coronal FIESTA image slices of the mouse body at day 21 post-implantation show the axillary node (solid arrow, A) and a massive tumor at the site of implantation (dashed arrow, B). In (C-G) images are cropped and enlarged to highlight the axillary node at days 1(C), 7 (D), 10 (E), 14 (F) and 21 (G) post-implantation. Signal loss appears in the axillary lymph node in images acquired on day 21.
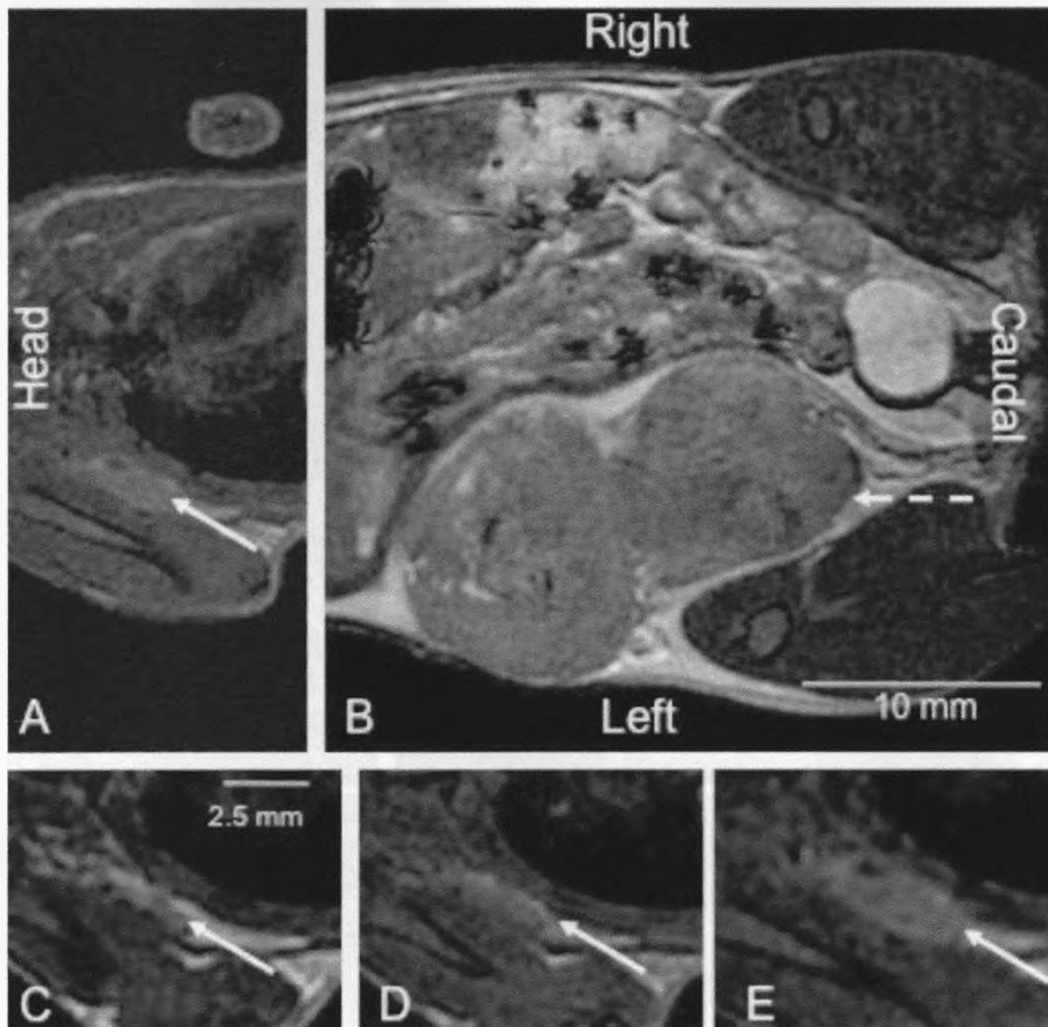
Figure 3.6: Appearance of Signal Loss Day 21 Post-Implantation Example 3

(A,B) Cropped coronal FIESTA image slices of the mouse body at day 21 post-implantation show the axillary node (solid arrow, A) and a massive tumor at the site of implantation (dashed arrow, B). In (C-E) images are cropped and enlarged to highlight the axillary node at days 1(C), 7 (D), and 21 (E). Signal loss appears in the axillary lymph node in images acquired on day 21. The axillary node could not be confidently identified in day 14 images.
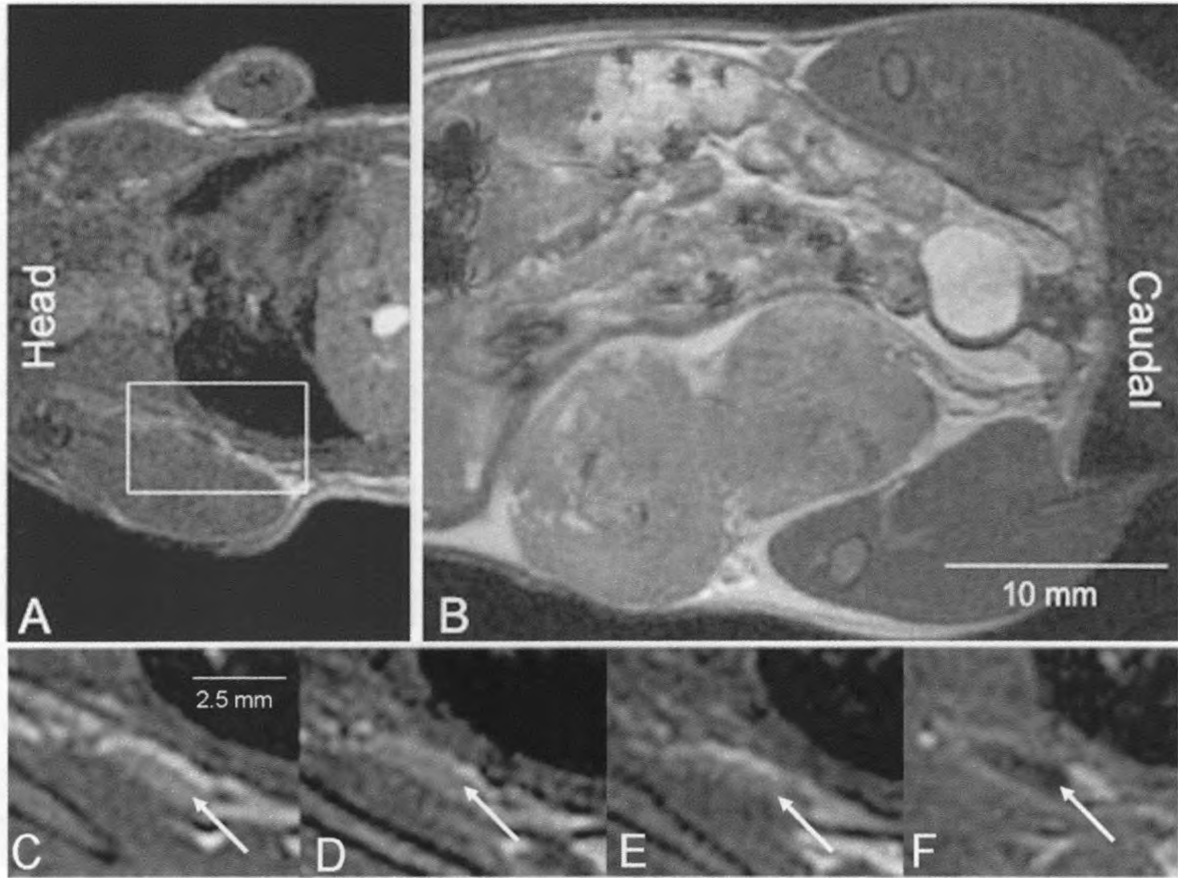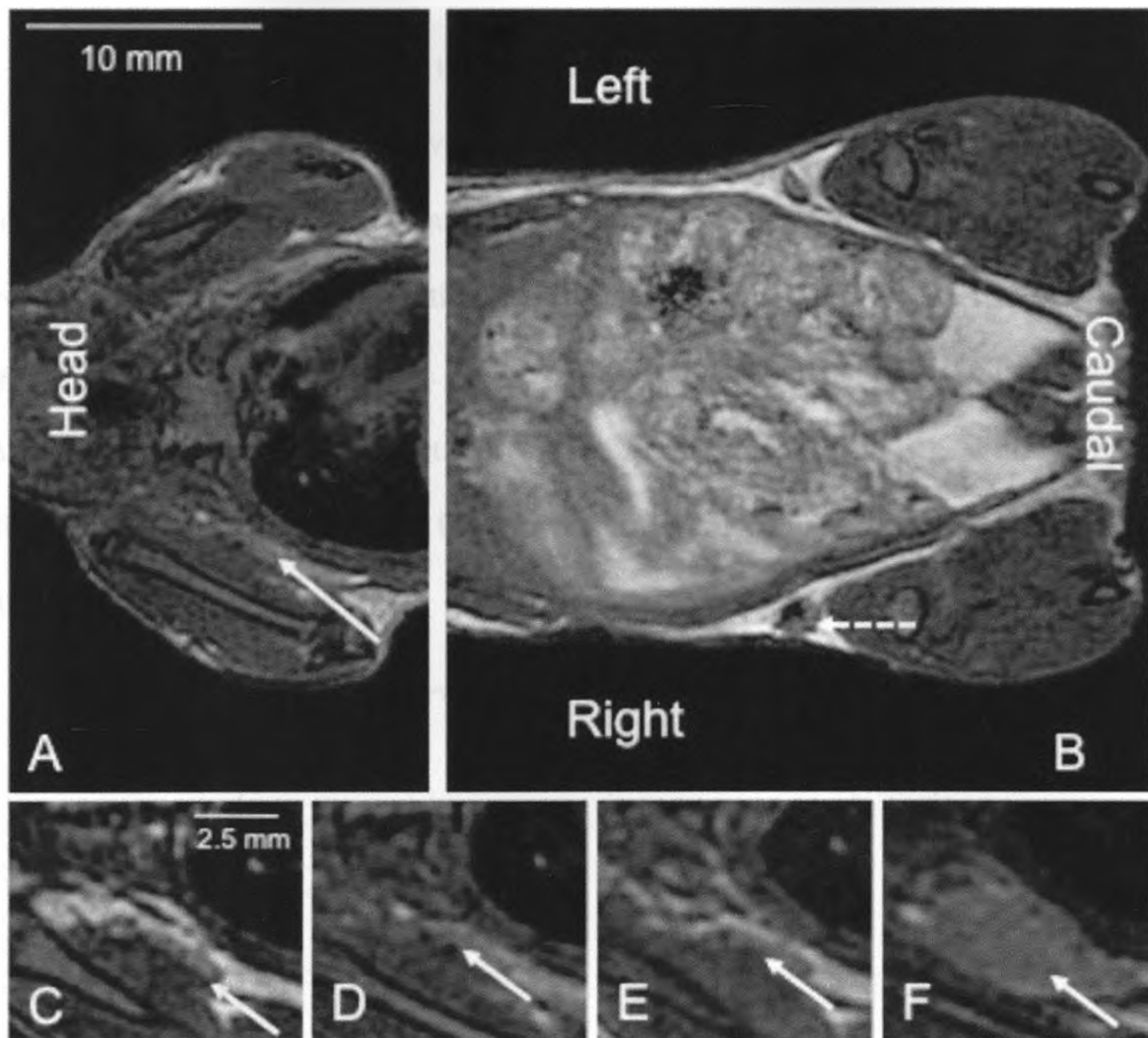
Figure 3.7: Appearance of Signal Loss Day 7 Post-Implantation

(A,B) Cropped coronal FIESTA image slices of the mouse body at day 7 post-implantation show the axillary node (solid arrow, A). The inguinal node looks enlarged after implantation of cells (dashed arrow, B). Signal loss can be clearly seen in the implant site. In (C-F) images are cropped and enlarged to highlight the axillary node at days 1(C), 7 (D), 14 (E), and 28 (F) post-implantation. Signal loss appears in the axillary lymph node in images acquired on day 7. The formation of a tumor is clearly visible on day 28. The axillary node could not be confidently identified in day 21 images.

For mice that were imaged until at least day 21 (24 of the 30 mice) tumor growth at the site of implantation was first evident in the images on day 7 in 8/24 mice, on day 10 in 3/24 mice, on day 14 in 9/24 mice and on day 28 in 2/24 mice. Growth curves for the tumors developing at the site of implantation are shown in Figure 3.8. The final tumor volumes ranged between $0.006 - 7.991$ cm^3. The size of the primary tumor at the implant site was not related to the size or number of metastases in the axillary node. The largest tumor measured at the axillary was found to be 0.151 cm^3 with a corresponding inguinal node volume of 0.006 cm^3.
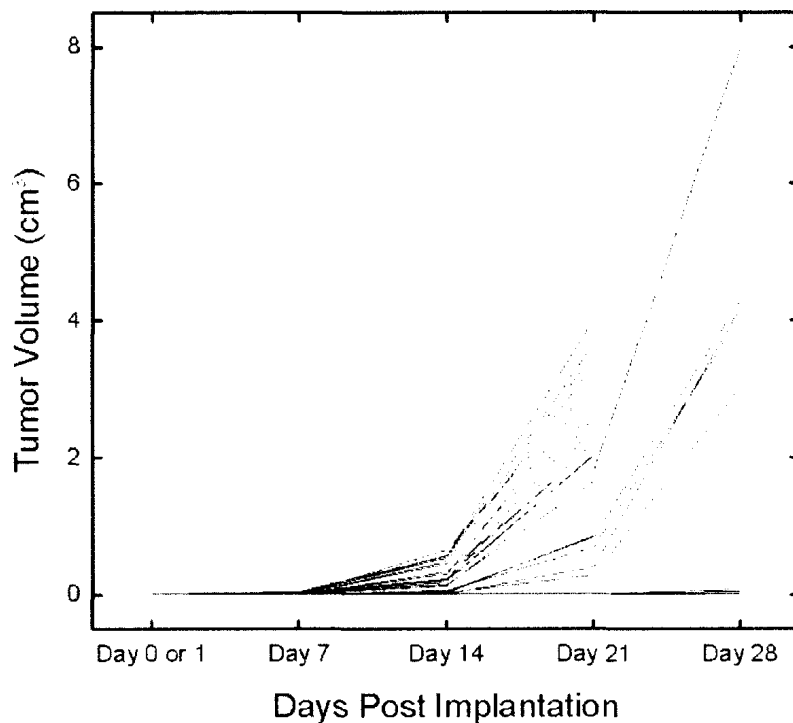
Figure 3.8: Tumor Growth Curves

Tumor growth curves of animals with an implantation of labeled cells in the right inguinal node that were imaged until day 21 or longer.

Figure 3.9 shows images of mice implanted with MPIO-labeled cells in the right inguinal node and unlabeled cells in the left inguinal node. Images at each time point where from a different animal. On day 0 post-implantation the presence of MPIO-labeled cells in the right inguinal node (3.9A) was obvious as a large region of signal loss while the appearance of the left inguinal node, implanted with unlabeled cells, was unchanged. On day 1 (3.9B,C) the development of tumors in both inguinal nodes can be seen, with signal loss persisting on the right side. On day 7 (3.9D,E), the signal in the developing tumors was more heterogeneous with areas of hyperintensity visible in both tumors, at this time point signal hypointensity was still only detected in the tumor on the right side where MPIO labeled cells were implanted. Day 14 (3.9F,G) images showed no appreciable difference between the tumors from labeled cells and tumors from unlabeled cells.
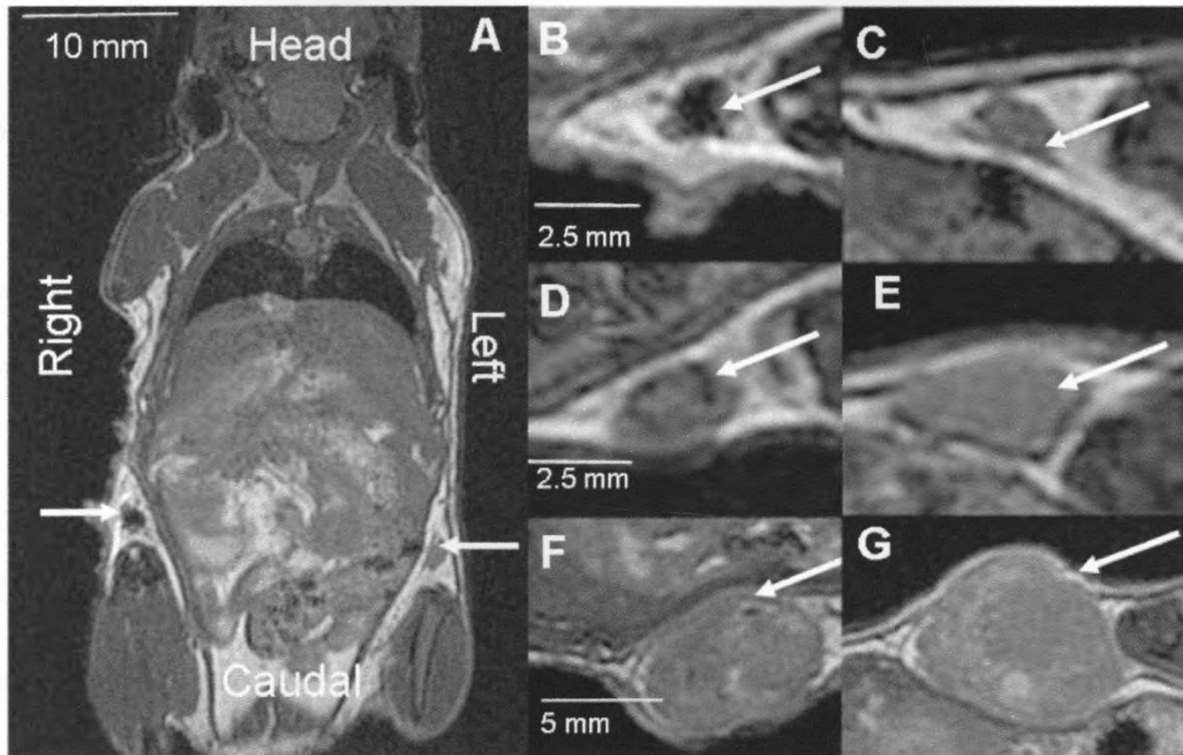
Figure 3.9: Progression of Tumors from Labeled and Unlabeled cells

(A) Sample coronal FIESTA image from a mouse implanted with iron-labeled B16F10 cells in the right inguinal node and unlabeled B16F10 cells in the left inguinal node. This image was acquired on day 0. In (B-G) images are cropped and enlarged to highlight both inguinal nodes at days 0 (B,C), 7 (D,E), and 14 (F,G) post-implantation. In this example signal loss is visible in the inguinal lymph node implanted with labeled cells on day 0 and persists until day 7. In images acquired on day 7, signal loss is not detected in the inguinal node implanted with unlabeled cells. Tumors at day 14 look similar, whether labeled or unlabeled cells were used.

3.3.3 Histology

PPB staining confirmed the presence of iron labeled cells within the inguinal tumors and within the axillary nodes (Figure 3.10). In the tumors that developed at the implantation site PPB staining was typically observed around the perimeter of the tumor and in connective tissue at the tumor tissue boarder. Large tumors showed areas of necrosis in H&E staining (not shown).

The axillary nodes from all mice that showed signal loss in the MR images were positive for iron. The degree of PPB staining observed in axillary nodes was greater than in the inguinal node/tumors. As with the inguinal nodes/tumors most of the PPB staining was observed along the perimeter of the tumor/node. The greatest amount of PPB staining was observed in axillary nodes scored as 'speckled' or 'micrometastatic'. In these cases, PPB staining was observed along the perimeter of the node as well as along the transverse sinuses within the paracortex.
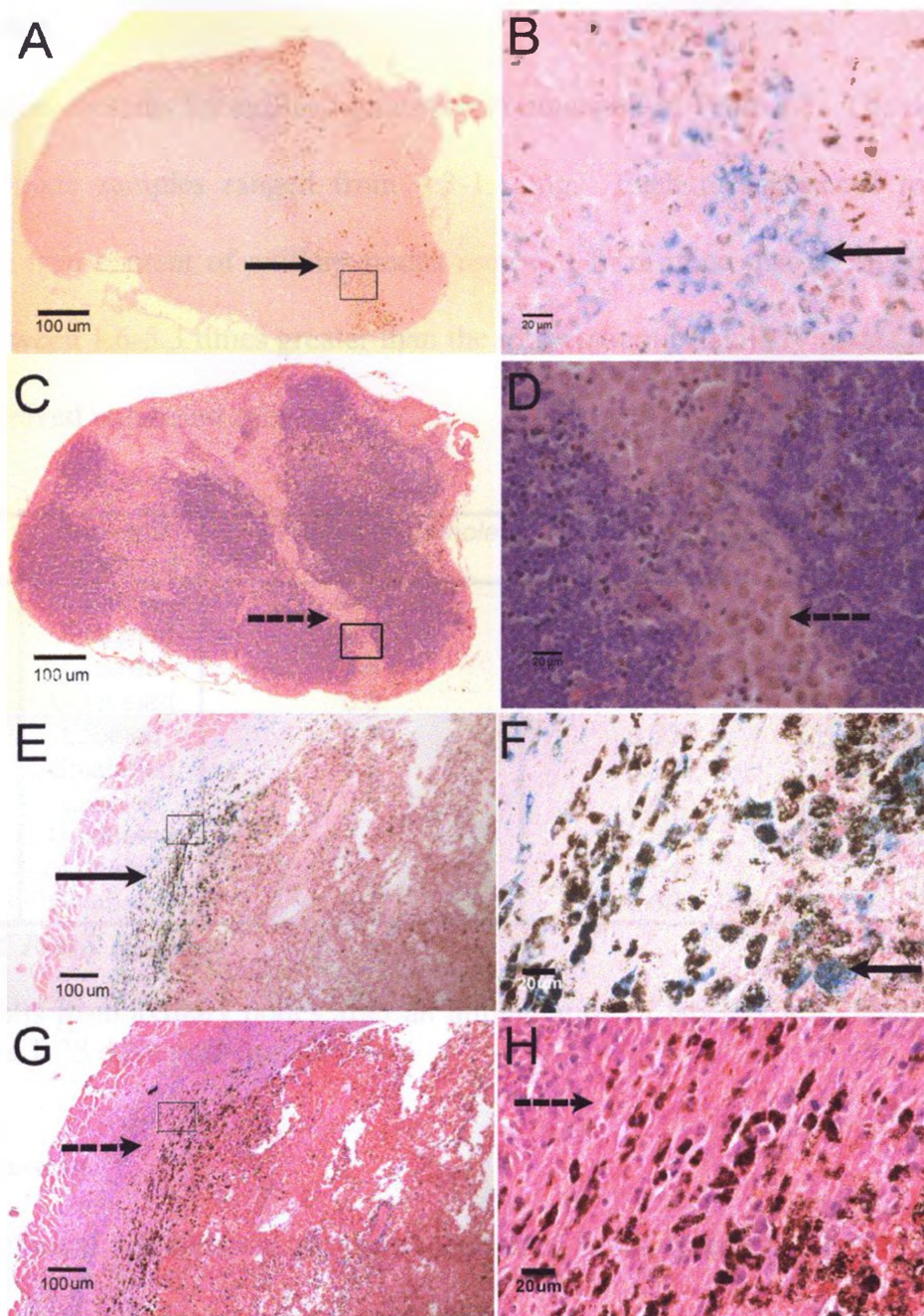
Figure 3.10: Histology of Tissues with Labeled Cells

A) PPB staining of an axillary node with signal loss appearing 21 days post-implantation of cells (4x magnification). Blue staining indicating the presence of iron is observed along the edge of the node and through the center. B) 40x magnification demonstrates blue staining inside brown melanin-producing cells indicating the presence of iron-labeled cells. C) H&E staining of the same node where the location of the sinus corresponds to the blue staining in the node shown in 6A (4x magnification). D) Melanoma cells are observed in the same location as blue stained cells in 6B (40x times magnification). E) PPB staining of the tumor at implant site. Iron can be seen along the perimeter of the tumor (4x magnification). F) At 40x magnification iron can be seen to be intracellular. G&H) H&E staining shows the boundary of the tumor and connective tissue (4x and 20x magnification respectively).

3.3.4 ICP-MS

The iron contents for axillary nodes are summarized in Table 3.1. The dry weights of

the axillary node samples ranged from 0.3-1.1 mg. Each measurement represents one

animal. The iron content of axillary nodes removed from mice that received iron-labeled

cells was between 1.6-5.3 times greater than the iron content of axillary nodes removed from

mice that received unlabeled cells.

Days post-implantation	Labeled/ Unlabeled	Dry Weight of Sample (mg)	Total Fe in Sample (µg)	Fe/mg of dry tissue (µg/mg)
1	Labeled	0.35	0.349	0.997
1	Unlabeled	0.3	0.097	0.323
7	Labeled	0.4	0.470	1.175
7	Unlabeled	0.6	0.182	0.303
14	Labeled	0.7	0.638	0.911
14	Unlabeled	0.5	0.168	0.336
21	Labeled	0.5	0.413	0.826
21	Unlabeled	1.1	0.366	0.333
28	Labeled	1	0.543	0.543
28	Unlabeled	6.7	0.691	0.103

Table 3.1: ICP-MS Results

ICP-MS results from axillary nodes after an implantation of labeled or unlabeled cells in the
inguinal node 1-28 days post-implantation.

3.4 Discussion

The clinical significance of micro-metastases in the lymph is a hotly debated topic,

but an improved understanding of the lymphatic spread of cancer remains important for

improving cancer survival. Advances towards understanding the interactions between tumor

cells and the lymphatic system have been, in part, limited by the lack of suitable noninvasive

assays and experimental models. Cellular MRI shows great promise as an imaging modality

to study metastasis. Previously, we developed MRI hardware and optimized pulse sequence

technology to allow the detection of single cells, labeled with MPIO particles, in-vivo in

mouse brain (28). This technology is applied here and in this study we have demonstrated

that MRI is capable of tracking spontaneous metastasis, to the best of our knowledge this has not been accomplished before.

The direct intranodal injection of metastatic melanoma cells provides a system for investigating regional tumor growth, cellular trafficking, and micro-metastatic progression. Even though the direct implantation of cells into the inguinal lymph node often resulted in the immediate movement of cells to the axillary node, this approach resulted in a reproducible research model. Metastatic melanoma occurred only in the lymphatic system, and only in the axillary node. By injecting a known number of cells into the lymph node, each animal started from a similar state. The fact that melanoma cells appeared in the axillary node on the same day of (or the day after) the implantation was likely the result of pressure in the lymphatic system. Real-time fluorescence imaging of mice which received an intranodal injection of human fibrosarcoma cells also showed that cells moved immediately from the inguinal to the axillary node (30). The fact that melanoma cells were present in the axillary node in many animals showed us that if metastasis to the axillary node occurred, we would be able to detect it. Previous work from our lab showed that the results of the intranodal implantation of B16F10 cells were very similar to the subcutaneous implantation of B16F10 cells in the flank, in terms of the size and incidence of tumors at the implant site and metastases to regional nodes (29).

Several studies have reported that MRI is useful for monitoring of tumors formed from iron-labeled cells and the impact of labeling cancer cells with SPIO has been tested extensively (31, 32). These studies have shown that cell viability, proliferation, apoptosis levels and the production of reactive oxygen species are not affected by SPIO labeling at the levels required for detection by MRI. Harisinghan et al. have now studied i.v. SPIO in

human cancer patients for detection of metastases in lymph nodes (33). In this study, we show that B16F10 cell viability and plating efficiencies are not different for MPIO-labeled versus unlabeled cells. In addition, MPIO labeling of B16F10 cells did not alter the incidence of tumor growth at the implant site or the number of distant nodes with disease.

There are some limitations of the use of MPIO for cancer cell labeling and tracking by MRI. First, all types of susceptibility artifacts will cause signal loss, including artifacts due to bone, vessels or local field inhomogeneities. This has the potential to cause false positives, leading to the incorrect identification of voids as iron-labeled cells. In this study the use of unlabeled cells as controls and the correlation of image data with PPB histology showed that signal loss in the distant node was a very good predictor of the presence of melanoma cells. All axillary nodes with signal loss regardless of day of appearance showed signs of disease at post-mortem. ICP-MS results demonstrated that there was at least a 60% increase in the amount of iron in the distant nodes with signal loss, which was only observed in animals with an implantation of labeled cells, when compared to animals with an implantation of unlabeled cells, where no signal loss was seen. ICP-MS results also demonstrated a high amount of iron in the normal control nodes. Since ICP-MS analysis measures all iron within the sample, the iron seen in normal nodes could be attributed to intranodal blood that could not be removed for measurements. This together with the observations that signal loss was not observed at the inguinal node after the implantation of unlabeled cells (until at least day 21) suggests that signal loss observed in images of the nodes can be attributed to the presence of iron-labeled cells. The development of new pulse sequences which generate positive contrast from iron-labeled cells, which is underway, may alleviate this concern (34).

Another issue is that the presence of free iron, that might be released from dead cancer cells, may be mistakenly reported as viable cells or that this iron might be taken up by macrophages, and similarly be incorrectly identified as the cells of interest. A recent paper by Pawelczyk et al., which studied iron uptake by bystander cells in an in vitro model system, indicates that the transfer of iron particles to macrophages, from dead, iron-labeled cells accounts for < 10% of the total iron in the labeled cells (35). This data advocates caution since the implantation of iron-labeled cells into tissues can result in uptake of label by macrophages, but suggests that the amount of iron in these cells may be quite low and that SPIO will be degraded by macrophages relatively quickly.

Perhaps the biggest potential limitation with the cellular imaging techniques implemented in this study is the fact that the MPIO label is expected to be diluted with cell division. In vitro studies by Arbab et al. showed that human mesenchymal stem cells, which are slowly dividing cells, retained the iron label for up to 7 weeks post cell labeling (32). Cancer cells divide quickly which should equate to a faster dilution of the contrast agent. Indeed, in the same study iron-labeled HeLa cells lost their iron label by 2-3 weeks post cell labeling and in our own experiments we have reported the dilution of the iron in B16F10 cells to below MR detectable levels in only 4-5 days post cell labeling (29). Our in-vivo data shows, however, that in a complex tumor system, the contrast from iron-labeled cells can persist for much longer than would be predicted by in-vitro cell division assays.

The ability to detect evidence of metastatic iron-labeled B16F10 cells in the axillary node, after implantation of these cells in the inguinal node, by histology, ICP-MS and MRI is intriguing. These observations suggest that there is something different about the metastatic phenotype that results in retention of the iron label. One explanation may be that these

metastatic cells are nonproliferative. Another interesting possibility is that these cells have properties of stem-like cells. It is exciting to consider that advanced cellular imaging techniques, as described in this paper, may be used to support a better understanding of the models of carcinogenesis and metastasis as well as potentially improve on the principles by which cancers are treated.

Future work may use *targeted* MR contrast agents. These contrast agents usually consist of iron-oxide particles joined to a ligand or antibody. Targeted contrast agents have been created by conjugating annexin V (36), folate acid (37), and $\alpha_v\beta_3$ integrin (38) to iron-oxide. These contrast agents have been shown to preferentially bind to apoptotic, cancer, and proliferating endothelial cells (a marker for angiogenesis) respectively and cause a change in relativity that can be detected in MR images as areas of hypointensity. MRI reporter genes have also been developed as a means of cell detection. Cancer cells have been transfected with the transferrin receptor, which increases the amount of cellular uptake of exogenously administered iron conjugated to a transferrin molecule (39). Endogenous reporters have also been developed where glioma cells are designed to overexpress ferritin. The cells then sequester free iron that is available in the body making them detectable with MRI (40). The development of these novel contrast agents will strengthen MRI's role in the study of metastasis.

3.5 References

1. Miller AJ, Mihm MC,Jr. Melanoma. N Engl J Med. 2006 Jul 6;355(1):51-65.

2. Grabau D, Jensen MB, Rank F, Blichert-Toft M. Axillary lymph node micrometastases in invasive breast cancer: National figures on incidence and overall survival. APMIS. 2007 Jul;115(7):828-37.

3. MacDonald IC, Chambers AF. Breast cancer metastasis progression as revealed by intravital videomicroscopy. Expert Rev Anticancer Ther. 2006 Sep;6(9):1271-9.

4. Cameron MD, Schmidt EE, Kerkvliet N, Nadkarni KV, Morris VL, Groom AC, et al. Temporal progression of metastasis in lung: Cell survival, dormancy, and location dependence of metastatic inefficiency. Cancer Res. 2000 May 1;60(9):2541-6.

5. Luzzi K, MacDonald IC, Schmidt EE, Kervliet N, Morris VL, Chambers AF, et al. Multistep nature of metastatic inefficiency: Dormancy of solitary cells after successful extravasation and limited survival of early mircometastasis. Am J Patho. 1998;153(3):865.

6. Weiss L. Comments on hematogenous metastatic patterns in humans as revealed by autopsy. Clin Exp Metastasis. 1992 May;10(3):191-9.

7. Rose PG, Piver MS, Tsukada Y, Lau TS. Metastatic patterns in histologic variants of ovarian cancer. an autopsy study. Cancer. 1989 Oct 1;64(7):1508-13.

8. Nathanson SD. Insights into the mechanisms of lymph node metastasis. Cancer. 2003 Jul 15;98(2):413-23.

9. Wu ZY, Li JH, Zhan WH, He YL, Wan J. Effect of lymph node micrometastases on prognosis of gastric carcinoma. World J Gastroenterol. 2007 Aug 14;13(30):4122-5.

10. Cserni G. Surgical pathological staging of breast cancer by sentinel lymph node biopsy with special emphasis on the histological work-up of axillary sentinel lymph nodes. Breast Cancer. 2004;11(3):242,9; discussion 264-6.

11. van Akkooi AC, de Wilt JH, Verhoef C, Schmitz PI, van Geel AN, Eggermont AM, et al. Clinical relevance of melanoma micrometastases (<0.1 mm) in sentinel nodes: Are these nodes to be considered negative? Ann Oncol. 2006 Oct;17(10):1578-85.

12. Li LL, Scolyer RA, Ka VS, McKinnon JG, Shaw HM, McCarthy SW, et al. Pathologic review of negative sentinel lymph nodes in melanoma patients with regional recurrence: A clinical study of 1152 patients undergoing sentinel lymph node biopsy. Am J Surg Pathol. 2003;27:1197-202.

13. Fink AM, Lass H, Hartleb H, Jurecka W, Salzer H, Steiner A. S-classification of sentinel lymph node predicts axillary nonsentinel lymph node status in patients with breast cancer. Ann Surg Oncol. 2008 Mar;15(3):848-53.

14. Roka F, Mastan P, Binder M, Okamoto I, Mittlboeck M, Horvat R, et al. Prediction of non-sentinel node status and outcome in sentinel node-positive melanoma patients. Eur J Surg Oncol. 2008 Jan;34(1):82-8.

15. Barrett T, Choyke PL, Kobayashi H. Imaging of the lymphatic system: New horizons. Contrast Media Mol Imaging. 2006 Nov;1(6):230-45.

16. Misselwitz B. MR contrast agents in lymph node imaging. Eur J Radiol. 2006 Jun;58(3):375-82.

17. Bulte JW, Kraitchman DL. Iron oxide MR contrast agents for molecular and cellular imaging. NMR Biomed. 2004 Nov;17(7):484-99.

18. Anzai Y. Superparamagnetic iron oxide nanoparticles: Nodal metastases and beyond. Top Magn Reson Imaging. 2004 Apr;15(2):103-11.

19. Moore A, Weissleder R, Bogdanov A,Jr. Uptake of dextran-coated monocrystalline iron oxides in tumor cells and macrophages. J Magn Reson Imaging. 1997 Nov-Dec;7(6):1140-5.
20. Weissleder R, Cheng HC, Bogdanova A, Bogdanov A,Jr. Magnetically labeled cells can be detected by MR imaging. J Magn Reson Imaging. 1997 Jan-Feb;7(1):258-63.

21. Josephson L, Lewis J, Jacobs P, Hahn PF, Stark DD. The effects of iron oxides on proton relaxivity. Magn Reson Imaging. 1988 Nov-Dec;6(6):647-53.

22. Neumaier CE, Baio G, Ferrini S, Corte G, Daga A. MR and iron magnetic nanoparticles. imaging opportunities in preclinical and translational research. Tumori. 2008 Mar-Apr;94(2):226-33.

23. Harisinghani MG, Barentsz J, Hahn PF, Deserno WM, Tabatabaei S, van de Kaa CH, et al. Noninvasive detection of clinically occult lymph-node metastases in prostate cancer. N Engl J Med. 2003 Jun 19;348(25):2491-9.

24. Kobayashi H, Kawamoto S, Brechbiel MW, Bernardo M, Sato N, Waldmann TA, et al. Detection of lymph node involvement in hematolgoic malignancies using micromagnetic resonance lymphangiography with a gadolinum-labeled nanoparticle. Neoplasia. 2005;7(11):984-91.

25. Choi SH, Han MH, Moon WK, Son KR, Won JK, Kim JH, et al. Cervical lymph node metastases: MR imaging of gadofluorine M and monocrystalline iron oxide nanoparticle-47 in a rabbit model of head and neck cancer. Radiology. 2006 Dec;241(3):753-62.

26. Weissleder R, Mahmood U. Molecular imaging. Radiology. 2001 May;219(2):316-33.

27. Modo M, Hoehn M, Bulte JW. Cellular MR imaging. Mol Imaging. 2005 Jul-Sep;4(3):143-64.

28. Heyn C, Ronald JA, Mackenzie LT, MacDonald IC, Chambers AF, Rutt BK, et al. In-vivo magnetic resonance imaging of single cells in mouse brain with optical validation. Magn Reson Med. 2006 Jan;55(1):23-9.

29. Foster PJ, Dunn EA, Karl KE, Snir JA, Nycz CM, Harvey AJ, et al. Cellular magnetic resonance imaging: In-vivo imaging of melanoma cells in lymph nodes of mice. Neoplasia. 2008 Mar;10(3):207-16.

30. Hayashi K, Jiang P, Yamauchi K, Yamamoto N, Tsuchiya H, Tomita K, et al. Real-time imaging of tumor-cell shedding and trafficking in lymphatic channels. Cancer Res.

31. Kalish H, Arbab AS, Miller BR, Lewis BK, Zywicke HA, Bulte JW, et al. Combination of transfection agents and magnetic resonance contrast agents for cellular imaging: Relationship between relaxivities, electrostatic forces, and chemical composition. Magn Reson Med. 2003 Aug;50(2):275-82.

32. Arbab AS, Bashaw LA, Miller BR, Jordan EK, Lewis BK, Kalish H, et al. Characterization of biophysical and metabolic properties of cells labeled with superparamagnetic iron oxide nanoparticles and transfection agent for cellular MR imaging. Radiology. 2003 Dec;229(3):838-46.

33. Harisinghani MG, Saini S, Weissleder R, Hahn PF, Yantiss RK, Tempany C, et al. MR lymphangiography using ultrasmall superparamagnetic iron oxide in patients with primary abdominal and pelvic malignancies: Radiographic-pathologic correlation. AJR Am J Roentgenol. 1999 May;172(5):1347-51.

34. Cunningham CH, Arai T, Yang PC, McConnell MV, Pauly JM, Conolly SM. Positive contrast magnetic resonance imaging of cells labeled with magnetic nanoparticles. Magn Reson Med. 2005 May;53(5):999-1005.

35. Pawelczyk E, Arbab AS, Chaudhry A, Balakumaran A, Robey PG, Frank JA. In vitro model of bromodeoxyuridine or iron oxide nanoparticle uptake by activated macrophages from labeled stem cells: Implications for cellular therapy. Stem Cells. 2008 May;26(5):1366-75.

36. Schellenberger EA, Bogdanov A,Jr, Hogemann D, Tait J, Weissleder R, Josephson L. Annexin V-CLIO: A nanoparticle for detecting apoptosis by MRI. Mol Imaging. 2002 Apr-Jun;1(2):102-7.

37. Sun C, Sze R, Zhang M. Folic acid-PEG conjugated superparamagnetic nanoparticles for targeted cellular uptake and detection by MRI. J Biomed Mater Res A. 2006 Sep 1;78(3):550-7.

38. Zhang C, Jugold M, Woenne EC, Lammers T, Morgenstern B, Mueller MM, et al. Specific targeting of tumor angiogenesis by RGD-conjugated ultrasmall superparamagnetic iron oxide particles using a clinical 1.5-T magnetic resonance scanner. Cancer Res. 2007 Feb 15;67(4):1555-62.

39. Weissleder R, Moore A, Mahmood U, Bhorade R, Benveniste H, Chiocca EA, et al. In-vivo magnetic resonance imaging of transgene expression. Nat Med. 2000 Mar;6(3):351-5.

40. Cohen B, Dafni H, Meir G, Harmelin A, Neeman M. Ferritin as an endogenous MRI reporter for noninvasive imaging of gene expression in C6 glioma tumors. Neoplasia. 2005 Feb;7(2):109-17.

Chapter 4 : Mammary Fat Pad Injection

4.1   Introduction

The experiments described in Chapter 3 show that after the intranodal implantation of cancer cells it is possible to track spontaneously metastasizing cells to the axillary lymph node with MRI. However, the imaging study also showed that in many cases signal loss, representing iron labeled cells, was observed in the axillary node on the first scan (day 0 or day 1 post-implantation). This finding likely represents the passive arrival of cells at the draining axillary node and not true metastasis. The work in this chapter describes a study designed to investigate another model of cell implantation for imaging metastasis – the implantation of melanoma cells into the mammary fat pad.

The mammary fat gland is often used to study cancer growth, especially for breast cancer where the mammary fat pad (MFP) is the site of the primary tumor (1). The implantation of a variety of different breast cancer cell lines in the MFP has resulted in metastasis to various tissues. Metastasis to the liver occurs when the murine mammary carcinoma cell line D2.0R and its variant D2A1 are implanted into the MFP (2). A rat adenocarcinoma (MTLn3) metastasizes to the axillary lymph node and the lung after MFP implantation (3) while the implantation of the murine mammary tumor cell line 4526 into the MFP results in metastasis to the lung, liver and heart (4). Here we have implanted B16F10 cells into the MPF. Though this is not the orthotopic site of tumor development for melanoma, others have also used the MFP as an implantation site for non-breast cancer cells. Lewis lung carcinoma implanted into the MFP was used to determine the effect of the

cyclooxygenase-2 inhibitor on recurrent tumor growth (5). An elevated level of parathyroid hormone-related peptide (PThrP), which can cause hypercalcemia and is a sign of malignancy, was measured in mice after the implantation of A375 (a human amelanotic melanoma cell line) in the MFP. By using the same cell line (B16F10) as in the previous chapters of this thesis, we can do a direct comparison of the metastatic potential of cells implanted at the MFP to those implanted intranodally.

Our goal was to develop a model, which would result in high numbers of metastases in the lymph nodes without the passive and instantaneous drainage of cells to the distant lymph nodes (which was observed with the intranodal implants). We hypothesized that the inguinal node would be the most common site of metastasis in this model because this is the first draining lymph node in the lower MFP. Metastasis to the inguinal lymph node would be also advantageous for imaging purposes since the inguinal lymph node is much easier to visualize with MRI, compared to the axillary lymph node.

In this study mice were implanted with B16F10 cells in the MFP and a post mortem analysis was used to evaluate the incidence of tumors at the implant site and metastatic spread to the lymph nodes. A pilot MRI study was included to follow a small group of mice that received iron-labeled cells.

4.2 Methods

4.2.1 Cell Labeling

Mouse melanoma cells (B16F10) were maintained in Dulbecco's modified Eagle's medium (DMEM) containing 10% Fetal Bovine Serum (FBS) at 37° C and 5% CO_2. Cells were plated in 6 well plates at 2.5×10^5 cells and 2 ml of media in each well. After 24 hours

the media was replaced with new media and 9.41×10^6 micron-size iron-oxide particles (MPIO, 0.9 μm diameter, Bangs Laboratory, Fishers, IN, USA) were added to each well. The cells were incubated with MPIO for 24 hours. Cells were washed 4 times with Hank's Buffered Salt Solution to remove any unincorporated iron. Cell viability was tested with the trypan blue exclusion and plating efficiency assays. After cell harvesting a subset of cells were diluted for injection and the remaining cells were kept in sterile conditions for plating efficiency assays. 100 cells were plated on a petri dish with 10 ml of media after all injections were completed. Cells were counted using a haemocytometer. The dish was monitored starting 7 days post plating for the appearance of cell colonies. The development of colonies occurred between 7-10 post plating. Once cell colonies were visible the media was removed from the dish and the colonies were fixed with 10% formalin for 10 minutes. After the removal of the formalin 0.5% cresyl violet blue was added to the dish for 5 minutes before the plate was rinsed with double distilled water. The numbers of colonies were then counted. Plating efficiency was found by the number of colonies counted divided by the number of cells plated.

4.2.2   Animal Model

C57Bl/6 mice (female, 6 weeks old, Charles River Laboratories, Wilmington, MA, USA) were anesthetized with the gas anesthetic isoflurane (1.5% in 100% oxygen). A small superficial incision was made to the abdomen right of the midline mammary fat pad. 10,000 or 50,000 B16F10 cells in 50 μl PBS were implanted directly into the mammary fat pad located beside the inguinal lymph node (30 gauge, Becton Dickinson Technologies). The wound was then closed with tissue glue (Vetbond, 3M company, St. Paul, MN).

There were 4 groups of mice used in this experiment. Group 1 received an injection of 10,000 labeled cells (n=5). Group 2 received an injection of 50,000 labeled cells (n=6). Group 3 received an injection of 10,000 unlabeled cells (n=4). Group 4 received an injection of 50,000 unlabeled cells (n=4).

4.2.3   Iron Content Measurements

Intracellular iron content was measured using a colorimetric assay. Three wells of a 96 well plate were each plated with 2.5×10^5 cells in 100 μl of HBSS. Samples with known concentrations of iron were also plated in triplicate to measure a calibration curve. The plate was then placed uncovered in an oven at 80°C overnight after which 100 μl of 5 M HCl was added to the samples. The plate was then covered and placed back into the oven for another 5 hours at 60°C. This was followed by the addition of 100 μl of 5% potassium fericynide to each well. After a 15 minute incubation in the dark, the plate was read on a spectrometer (λ=650 nm, Vmax, Molecular Devices, Sunnyvale, CA). Iron content was calculated using the calibration curve and the known cell concentration.

4.2.4   Statistical Analysis

The student t-test was performed to compare the number of nodes with metastasis between the two cell count groups and between the intranodal and MFP model using Microsoft Excel 2002 (Microsoft, Redmond, WA, USA).

4.2.5   MRI

Imaging was performed on a 1.5T GE CV/I whole body clinical MR scanner using a custom-built, insertable gradient coil (inner diameter=17.5 cm, maximum gradient strength=500 mT/m, and peak slew rate= 3000 mT/s) and a custom-built mouse body radiofrequency coil (inner diameter= 4 cm). Anesthesia was induced and maintained with isoflurane (1.5 % in 100% oxygen) delivered to the animals via a nose cone and scavenged by vacuum. Mice were kept warm during the scanning with the use of heated water pads. Images of the whole mouse body were acquired using the 3D fast imaging employing steady state acquisition (3D-FIESTA) pulse sequence. The imaging parameters were: repetition time = 9.2ms, echo time = 4.1ms, flip angle = 30°, 2 signal averages, spatial resolution = 200 μm^3 isotropic, scan time = 23 minutes. All MRI images were assessed for regions of signal loss in the mammary fat pad and in draining lymph nodes (inguinal and axillary lymph nodes).

4.2.6   Post Mortem Analysis

All animals underwent a post-mortem examination by dissection. Melanoma cells and tumors were easily visualized by the brown pigmentation produced by melanin. Nodes were classified as follows: "Speckled" which characterized sparse areas of discolouration on the surface of the node that indicated the presence of cells in the node but had not yet developed into a tumor mass, "micro" which indicated dot-like tumor mass(es) on the surface of the lymph node, "small" describes tumor foci that was <50% of the total nodal surface and "large" describes tumor foci that had taken over the entire node or is ≥50% of the total nodal surface. Growths at the site of implantation were referred to as "tumors".

4.3 Results

4.3.1 Cell Culture

The trypan blue exclusion assay showed that 98% of labeled cells and 98% of unlabeled cells were viable after harvesting. Plating efficiency results showed for labeled and unlabeled cells an efficiency of 74% and 82.5% respectively (each from an average of two plates). The average iron content was found to be 57.8 pg of Fe/cell.

4.3.2 Post Mortem

9/10 of the animals with an injection of 50,000 cells, labeled or unlabeled, had tumors at the implant site. The one animal that did not develop tumor was a mouse injected with 50,000 unlabeled cells. 5/9 animals injected with 10,000 cells developed tumors at the implant site. 3 animals without tumors at the implant site were mice injected with 10,000 unlabeled cells and the remaining animal was injected with 10,000 labeled cells. Tumors which developed at the site of implantation after an implantation of 50,000 cells were larger than those of animals with an implantation of 10,000 cells. The size distribution of the tumors are shown in Table 4.1.

Weight Range (g)	10,000 cell implantation	50,000 cell implantation
0-0.99	4	1
1-2.99	2	1
3-4.99	3	2
5-6.99	0	2
>7	0	4

Table 4.1: Tumor Weight Ranges

The majority of nodes with metastasis were the axillary nodes. Two animals with an implantation of 10,000 cells had metastases that were found in the inguinal. One of these animals did not develop a tumor at implant site but had metastasis in both the axillary and inguinal nodes. The other animal did develop a tumor at the implant site and also had disease in the inguinal and axillary nodes. In the remaining animals with tumor development at the implant site, the inguinal lymph node was not recoverable. No metastatic growths were observed in other nodes or organs in the mice. Table 4.2 summarizes the number of tumors found post-mortem at the implant site and the total number of animals with metastases within each group. The number of animals with disease in the distant nodes did was not significantly different (p=0.54) between the two count groups.

Group	Sample Size	# of animals with tumors at implant site	# of animals with metastases
50,000 labeled	6	6	6
50,000 unlabeled	4	3	2
10,000 labeled	5	4	5
10,000 unlabeled	4	1	1

Table 4.2: Incidences of Tumors at Implant Site and Metastases

Table 4.3 lists the grade of all metastatic nodes found at post-mortem from the two groups with different numbers of cells implanted in the MFP. Each column consists of both labeled and unlabeled cells. All nodes are axillary nodes with the exception of the two large inguinal nodes found in the 10,000 cell group.

# cells implanted Grade	10,000 Cells	50,000 Cells
Speckled	5	5
Micrometastases	1	1
Small metastases	0	2
Large metastases	2	0

Table 4.3: Grading Scale for Nodes with Metastases

4.3.3 Imaging

Four mice were imaged. Two mice from group 1, which received an implantation of 10,000 labeled cells and two mice from group 2, which received an implantation of 50,000 labeled cells, were imaged on days 1, 7, 14, and 21 (one mouse from group 1 did not get a day 1 scan).

Signal hypointensity was observed on day 1, in the mammary fat pad near the inguinal lymph node, in 1 of the 2 mice which received an implantation of 10,000 cells and in both mice which received 50,000 cells. Figure 4.1 shows a sequence of images from days 1-21 from an animal after an injection of 10,000 cells. In this mouse, signal loss was not observed in either the axillary (dashed arrow) or inguinal node (double-lined arrow) and no tumor growth was evident at the site of implantation.
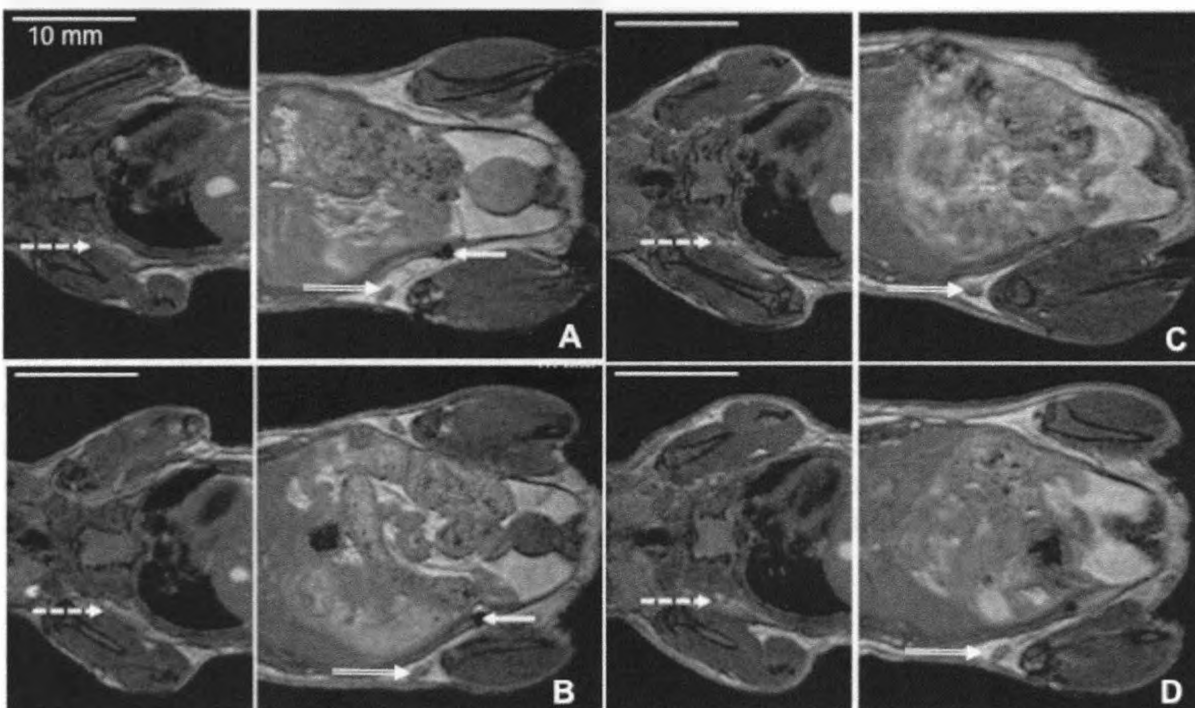

Figure 4.1: Implantation of 10,000 Cells in MFP without Tumor Growth

A dense area of signal loss (solid arrow) is visible on day 1 (A). Signal loss persists until day 7 (B). By day 14 (C) the region of signal loss at the implant site had disappeared. No signal loss or tumor formation can be seen on day 21 (D).

The second animal with an implantation of 10,000 cells that was imaged from day 7-21 showed tumor growth on day 7 of imaging. Signal loss persisted at the implant site in this animal until day 21 (Figure 4.2). Signal loss was also seen in the axillary node 21 days post-implantation of cells. The node appeared "speckled" with brown pigmentation upon gross dissection.
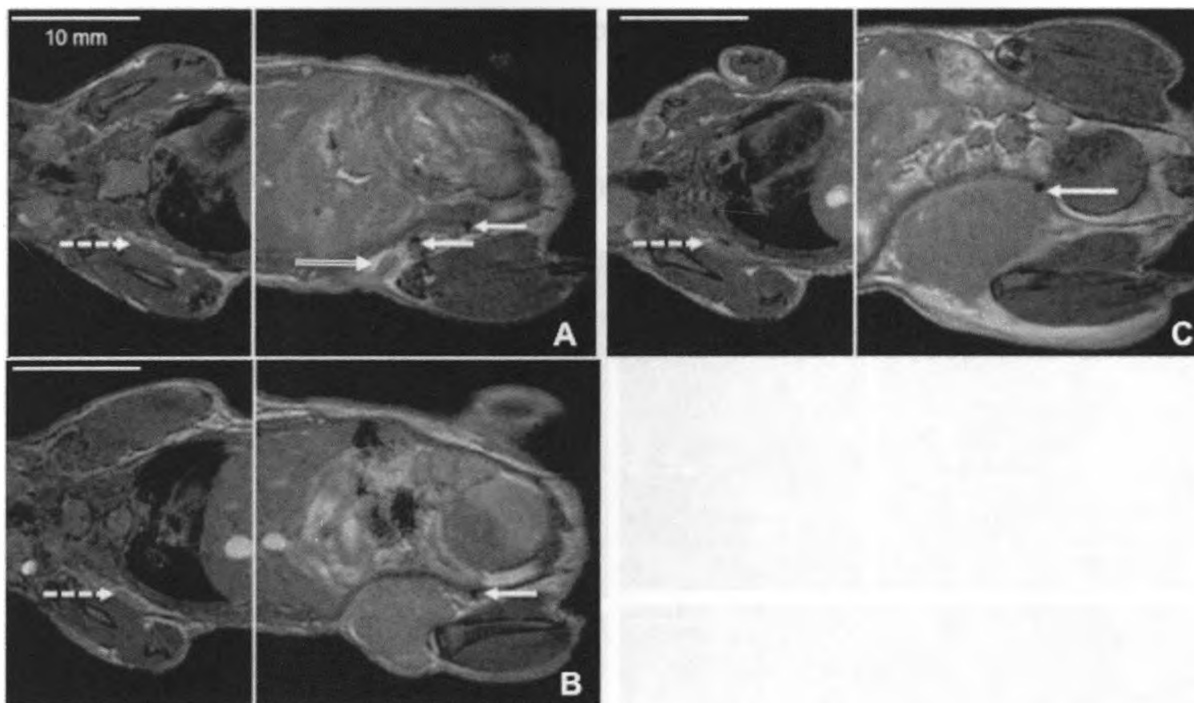
Figure 4.2: Implantation of 10,000 cells in MFP with Tumor Growth

(A) Day 7 images show two distinct areas of signal loss (solid arrows), one within the developing tumor and one at the abdominal wall boundary. The axillary node (dashed arrow) and inguinal node (double lined arrow) do not have signal loss. (B) There remains one area of signal loss on day 14 and signal loss is still not observed in the axillary node. (C) Images acquired on day 21 reveal signal hypointensity at the axillary node.

Both animals implanted with 50,000 cells had tumor development at the injection site by day 7. Figure 4.3 shows images from an animal with a 50,000 cell implantation. Signal loss persisted from days 1-21 at the implant site. Signal loss was also seen in the axillary node of this animal 21 days post-implantation of cells. At dissection a micrometastasis was found in the axillary node. Figure 4.4 shows the second animal with a 50,000 cell implantation. Signal loss at the implant site only persisted till day 14. This animal also had signal loss appear in the axillary node 21 days post-implantation of cells. Upon dissection a small metastases was found in the axillary node.
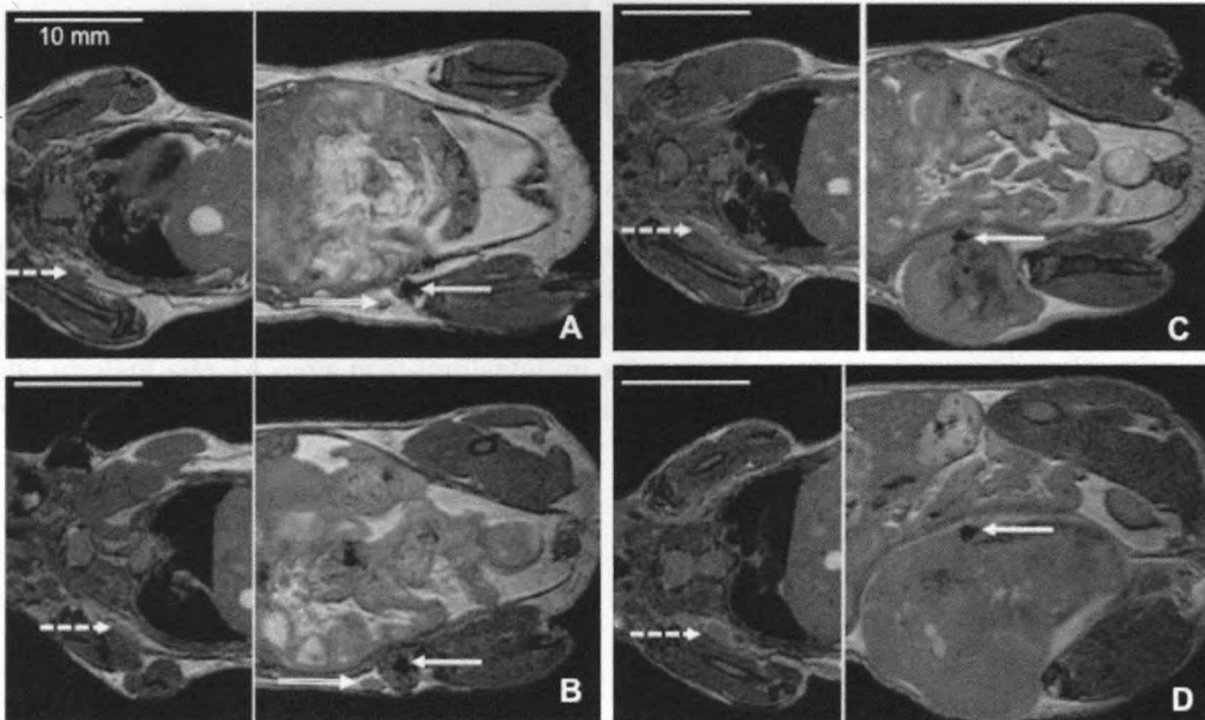
Figure 4.3: Implantation of 50,000 in MFP Labeled Cells

(A, B, C) Dense signal loss was observed in Day 1, 7, and 14 images at the implant site while the inguinal (double lined arrow) and the axillary node (dashed arrow) could also be observed (though not seen in the specific day 14 image above). (D) Signal loss persisted in the tumor on day 21 though the inguinal node could not longer be observed. The axillary node also showed hypointensity on day 21 images.
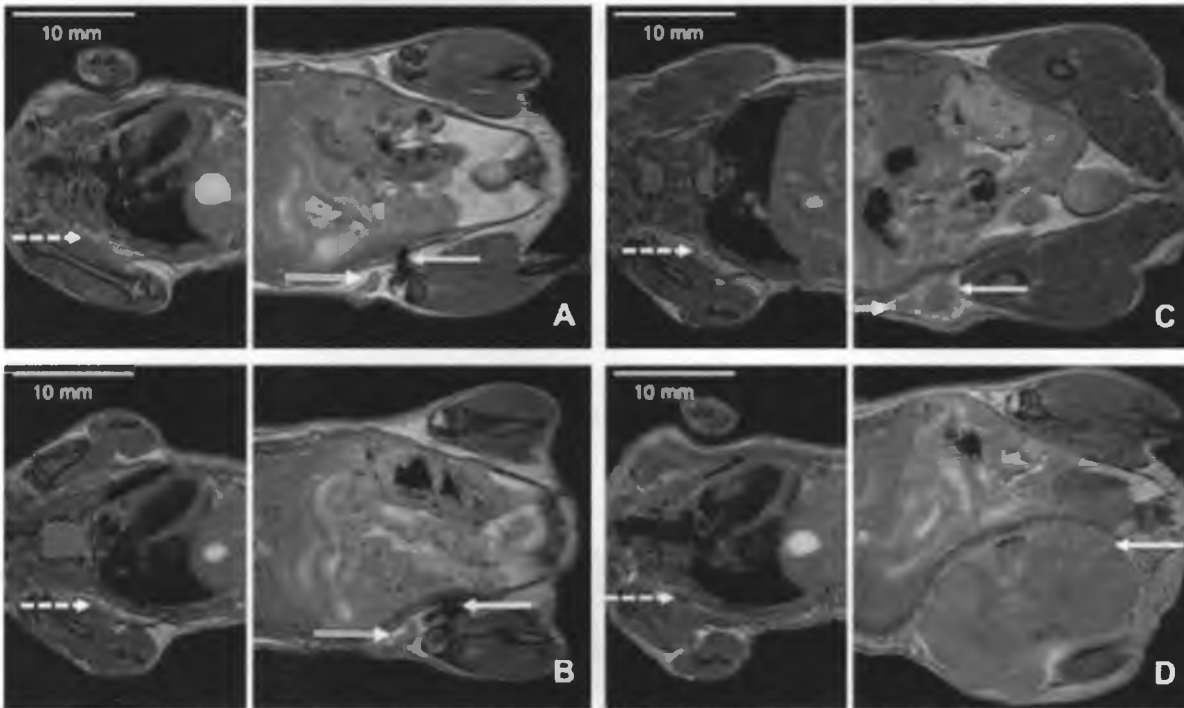
Figure 4.4: Implantation of 50,000 cells in MFP in Second Animal

(A) Day 1 images show a large area of signal loss (solid arrow) at the site of implantation, adjacent to the inguinal lymph node (doubled-lined arrow). (B) Day 7 images showed a diminished region of signal loss at the implant site. (C) Signal loss was no longer visible at the implant site 14 days post-implantation after the formation of a tumor. (D) Signal loss was observed in the axillary node day 21 post-implantation (dashed arrow).

Signal loss was seen in the axillary node in 3 of the 4 animals that were images. The

one animal without signal loss in the axillary node was from an animal with an implantation

of 10,000 cells. All signal loss in the axillary node was seen 21 days post-implantation of

cells. All 3 animals showed signs of disease upon post-mortem suggesting that cells arrived

at the node between days 14 and 21 post-implantation. Figure 4.5 contain the images of the

axillary nodes from days 1-21 with visible signal loss.
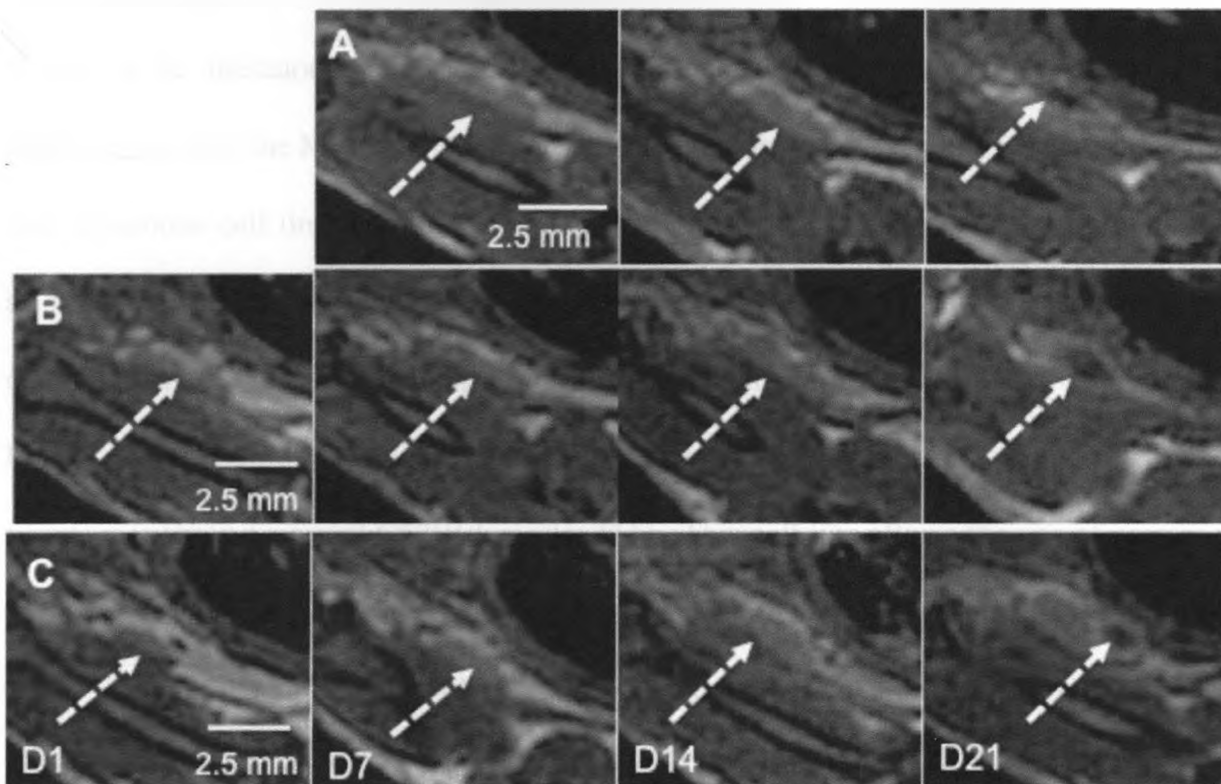

Figure 4.5: Axillary Nodes with the Appearance of Signal Loss

(A) Images of the axillary node (the dashed arrow) from days 7-21 in the animal with a
10,000 implantation of labeled cells. Signal loss not visible till day 21. (B,C) The axillary
node (dashed arrow) of both animals with a 50,000 cell implantation from days 1-21. Signal
loss was observed 21 days post-implantation of cells.

4.4 Discussion

There are numerous models of lymphatic metastasis that employ various cell lines. By using the selective techniques first introduced by Fidler in 1973 (6), Vantyghem et al. isolated a variant from the cell line MDA-MB-468, a human breast adenocarcinoma cell line, that aggressively metastasized to the lymphatics. The MDA-MB-468LN line metastasizes to axillary, cervical, periscapsular, peri-tracheal, per-aortic, inguinal, mammary fat pad, peri-renal, and pelvic lymph nodes at 12 weeks post-injection into the MFP (7). MDA-MB-435, which historically has been thought to be a breast cancer cell line but has recently been shown to be melanocytic in origin (8), also metastasizes to the lymph nodes after an implantation into the MFP (9). An aggressive squamous cell carcinoma variant of the human oral squamous cell line 686 has been established that metastasizes to the lymph nodes after an implantation into the submandibular to mylohyoid muscle (10). These models produce consistent metastases in the lymph nodes. The examples described above use human cell lines and require immune compromised mice for in-vivo studies. The B16 cell line arose spontaneously in a normal C57Bl/6 mouse (11). This cell line allows the use of normal mice with intact lymphatic systems, representing a truer microenvironment faced by cancer cells.

The implantation of B16F10 cells into the MFP is a promising model for imaging metastasis in the lymphatic system. Signal loss was not detected in the nodes on day 1 of scanning, as we observed with the direct intranodal implantation. In the mice with an implantation of 10,000 cells (both the labeled and unlabeled groups) in the MFP, it was determined that approximately 56% of mice had metastases in the axillary node. This is a higher percentage when compared to the 20% of mice that showed "real" metastases (where signal loss was seen in the axillary node several days post-implantation and had signal loss in

the axillary node at post mortem) in the intranodal model from Chapter 3. The difference in the occurrence of metastasis between the MFP and the intranodal model with the same number of implanted cells was found to be significantly different (p=0.01). 80% of mice implanted with 50,000 (labeled and unlabeled) cells had axillary nodes with metastases. The actual number of metastatic nodes were the same for both groups because of two animals in the 10,000 group developed metastasis in both the inguinal and axillary nodes. The percentage of animals with metastasis in 50,000 cells group was larger than that of the 10,000 cells group but not significantly so.

The issue of implanting melanoma cells into the mammary fat pad of the mouse might be curious to some. Although the mammary fat pad is not the orthotopic site for tumor development in melanoma, they both display the same chemokine receptors that are related to cancer metastasis. Recent evidence has emerged that chemokines may play a role in key role in several steps of metastasis including cell arrest, migration, and angiogensis (12). Both breast cancer and melanoma cells express the CXCR4 receptor, whose expression is low or absent from normal tissues and promotes metastasis to the lung, bone, and lymph nodes. The CCR7 receptor, also shown to promote lymphatic metastasis, is also present in both breast cancer cells and melanoma (13). These similarities demonstrate that the implantation of melanoma cells in the mammary fat pad is not such an inaccurate model of metastasis and that it could be used for further studies into metastasis.

A limitation of this model was that tumors in the MFP developed more quickly than intranodal tumors, causing a premature endpoint to the experiment; all animals were sacrificed before the planned endpoint of 28 days post cell implantation. Most axillary nodes with metastasis in both groups were graded as being "speckled". This suggests that tumor

growth was at an early stage or that cells in the axillary node were nonproliferative. To test whether metastatic tumors would develop in the axillary nodes in this model future work will consider implantation of cell numbers between 10,000 and 50,000 and/or the resection of the tumor that is developing at the implantation site.

4.5 Conclusion

The MFP model looks to be a better model for imaging spontaneous metastasis in the lymphatic system, compared to the intranodal implantation model. Cellular MRI techniques can be used to track cells migrating to distant lymph nodes in the MFP model.

4.6   References

1. Medina D. The mammary gland: A unique organ for the study of development and tumorigenesis. J Mammary Gland Biol Neoplasia. 1996 Jan;1(1):5-19.

2. Naumov GN, MacDonald IC, Weinmeister PM, Kerkvliet N, Nadkarni KV, Wilson SM, et al. Persistence of solitary mammary carcinoma cells in a secondary site: A possible contributor to dormancy. Cancer Res. 2002 Apr 1;62(7):2162-8.

3. Matsuda H, Strebel FR, Kaneko T, Stephens LC, Danhauser LL, Jenkins GN, et al. Apoptosis and necrosis occurring during different stages of primary and metastatic tumor growth of a rat mammary adenocarcinoma. Anticancer Res. 1996 May-Jun;16(3A):1117-21.

4. Hossain A, Sarkar NH. Colonization characteristics of a murine mammary tumor cell line that metastasizes frequently to the heart. Clin Exp Metastasis. 1991 Jul-Aug;9(4):351-61.

5. Qadri SS, Wang JH, Coffey JC, Alam M, O'Donnell A, Aherne T, et al. Surgically induced accelerated local and distant tumor growth is significantly attenuated by selective COX-2 inhibition. Ann Thorac Surg. 2005 Mar;79(3):990,5; discussion 990-5.

6. Fidler IJ. Selection of successive tumor lines for metastasis. Nat New Biol. 1973 Apr 4;242(118):148-9.

7. Vantyghem SA, Allan AL, Postenka CO, Al-Katib W, Keeney M, Tuck AB, et al. A new model for lymphatic metastasis: Development of a variant of the MDA-MB-468 human breast cancer cell line that aggressively metastasizes to lymph nodes. Clin Exp Metastasis. 2005;22(4):351-61.

8. Ellison G, Klinowska T, Westwood RF, Docter E, French T, Fox JC. Further evidence to support the melanocytic origin of MDA-MB-435. Mol Pathol. 2002 Oct;55(5):294-9.

9. Meschter CL, Connolly JM, Rose DP. Influence of regional location of the inoculation site and dietary fat on the pathology of MDA-MB-435 human breast cancer cell-derived tumors grown in nude mice. Clin Exp Metastasis. 1992 May;10(3):167-73.

10. Zhang X, Liu Y, Gilcrease MZ, Yuan XH, Clayman GL, Adler-Storthz K, et al. A lymph node metastatic mouse model reveals alterations of metastasis-related gene expression in metastatic human oral carcinoma sublines selected from a poorly metastatic parental cell line. Cancer. 2002 Oct 15;95(8):1663-72.

11. Teicher BA. Tumor models in cancer research. Totowa, N.J.: Humana Press; 2002.

12. Kakinuma T, Hwang ST. Chemokines, chemokine receptors, and cancer metastasis. J Leukoc Bio. 2006 Apr;79(4):639-51.

13. Müller A, Homey B, Soto H, Ge N, Catron D, Buchanan ME, et al. Involvement of chemokine receptors in breast cancer metastasis. Nature. 2001 Mar 1;410(6824):50-56

Chapter 5 : Summary, Conclusions and Future Directions

5.1   Summary and Conclusions

Chapter 2 of this thesis examined the differences between tumor development at the implant site and the resulting metastatic development in distant nodes in two tumor models: the subcutaneous implantation of cells in the flank, a more traditional model of melanoma metastasis, and the intranodal implantation of cells, where cells were injected directly into the inguinal lymph node.   The effect of a MR contrast agent, micron size iron-oxide particles, on the growth of the cells was also investigated.   The results showed no difference in metastatic potential or plating efficiency between the labeled and unlabeled cells.   The occurrence of disease in the distant lymph nodes between the two implant sites were similar and the decision of which model was better suited for our goals was based on the manner in which the tumors developed.   Tumors from the subcutaneous implantation grew outward, affecting the animal's mobility and making it difficult to fit mice into the mouse body RF coil used for imaging.   Metastasis was contained to the axillary node in the intranodal model, which is beneficial for cell tracking.   Therefore it was concluded that the intranodal model was more appropriate for MR imaging studies.

The feasibility of tracking metastatic cancer cells in the lymphatic system using our cellular MRI techniques was investigated in Chapter 3.   Using the intranodal model and comparing groups implanted with labeled, unlabeled, or both cell types into the inguinal lymph node(s) several observations were made.   The most important finding was that spontaneous metastases could be imaged using cellular MRI techniques.   Images showed

areas of signal loss within the axillary lymph node several days post-implantation, which corresponded to the presence of melanoma cells in the node. ICP-MS results showed that there was more iron in the axillary nodes from mice implanted with iron-labeled cells (and with signal loss in the axillary node identified by MRI) than in axillary nodes from mice implanted with unlabeled cells.

Another interesting finding was that the implantation of cells into the inguinal node resulted in the direct passage of cells to the axillary lymph node, possibly as a result of an increase in pressure due to the injection volume itself. This occurred in the majority of animals with signal loss in the distant node. This result, while initially unwanted, provided a means of evaluating the MR detection limits. We were able to show that if iron labeled cells were present in the axillary node, despite how they arrived there, that we could visualize them with MRI. The axillary node was more difficult to detect in MR images compared to other nodes, such as the inguinal nodes. Since the inguinal node is located in the fat pad there is high contrast between the node tissue and its surroundings. The axillary node is situated between fat and muscle thus the contrast between the axillary node and its surroundings is not as high. These two factors pointed to the need for a model of metastasis which would better facilitate imaging studies of true metastasis. This was the motivation for testing the mammary fat pad as an implantation site in Chapter 4.

In Chapter 4 melanoma cells were implanted into the mammary fat pad near the inguinal node. Labeled and unlabeled cells were compared, as well as two different cell counts (10,000 or 50,000). Post-mortem results showed a high incidence (8/10 animals) of axillary node metastasis in animals with an implantation of 50,000 cells. Within the subset of animals that were imaged, 3/4 animals showed signal loss in the axillary node 21 days

post-implantation. This result was promising since no signal loss was observed on day 1 of imaging suggesting that the passive drainage of cancer cells due to mechanical pressure alone does not occur at this implant site. It was expected that there would also be metastasis to the first draining lymph node, the inguinal node, however the tumors grew quickly and overtook the inguinal node. As a result the inguinal node was indistinguishable from tumor tissue. The larger tumors also prevented the monitoring of the animals beyond day 24 and the majority of the axillary nodes with disease were "speckled". Despite this, the mammary fat pad looks like a promising implantation site for imaging metastasis in the lymphatic system because of the very high incidence of axillary node metastases.

We have shown here that for the first time, that imaging spontaneous metastasis is possible with cellular MRI. Several stages of carcinogenesis were observed by MRI including the development of a tumor at the implant site, the arrival of cells at distant lymph nodes before the formation of a secondary tumor, and tumor development at the distant lymph node. Cellular MRI is unique in its ability to differentiate between soft-tissue, is depth independent, its ability to provide large fields of view. Moreover, MRI can be used to image a small number of cells (with the assistance of contrast agents) and is a non-invasive and safe imaging modality with no known side effects, making this the optimal technology to study metastasis.

5.2 Future Work

The preliminary work involving the mammary fat pad implantation has been shown to be a more successful model of cancer to the lymphatics. However, the number of cells implanted needs to be optimized. Also, the effect of resection of the tumor at the implant

site should also be studied in order to determine whether signal loss observed at the distant node represents active cells. The resection of the tumor at the implant site would delay the endpoint of the experiment and potentially give the cells in the axillary node time to progress. If the mammary fat pad is to be used as the model of choice, then a change in the cell line should be considered. The mammary fat pad implantation site is the orthotopic site for breast cancer. Using breast cancer cells would provide a more applicable model of cancer metastasis to the lymph nodes at this implant site.

Imaging with a larger sample group for the mammary fat pad model should be conducted to determine whether the metastasis observed in the axillary lymph node is always associated with iron-labeled cells. This should be followed by a more in-depth study into the cells themselves. Cells that retain their iron and cause signal loss in the distant node should be harvested to determine the characteristics unique to these cells compared to the general population of cells.

In the more distant future the use of more sophisticated contrast agents should be implemented. The dilution of transient contrast agents, which is especially troublesome in rapidly dividing cells like cancer cells, can be eliminated by the use of targeted contrast agents or the use of reporter genes. Of the two methods, reporter genes would be the most beneficial since no exogenous iron needs to be administered and it eliminates the problem of imaging free iron. This would enable the tracking of cells throughout the whole body without the time constraints associated with dilution of the contrast agent or issues with specificity associated with targeting agents.

Appendices

Western

This is the Original Approval for this protocol
A Full Protocol submission will be required in 2010

Dear Dr. Foster:

Your Animal Use Protocol form entitled:

Evaluation of Iron Labeled Melanoma Cells Injected into the Mouse Lymph Node Using MRI
Funding Agency CIHR - Grant MOP-57916

has been approved by the University Council on Animal Care. This approval is valid from **March 16, 2006 to March 31, 2007.** The protocol number for this project is 2006-013-03 .

1. This number must be indicated when ordering animals for this project.
2. Animals for other projects may not be ordered under this number.
3. If no number appears please contact this office when grant approval is received.
   If the application for funding is not successful and you wish to proceed with the project, request that an internal scientific peer review be performed by the Animal Use Subcommittee office.
4. Purchases of animals other than through this system must be cleared through the ACVS office. Health certificates will be required.

ANIMALS APPROVED FOR 1 YR.

Species	Strain	Other Detail	Pain Level	Animal # Total for 1 Year
Mouse	C57Bl/6	14-20 gm M/F	C	24

STANDARD OPERATING PROCEDURES
Procedures in this protocol should be carried out according to the following SOPs. Please contact the Animal Use Subcommittee office (661-2111 ext. 86770) in case of difficulties or if you require copies.
SOP's are also available at http://www.uwo.ca/animal/acvs
310 Holding Period Post-Admission
320 Euthanasia
321 Criteria for Early Euthanasia/Rodents
330 Post-Operative Care/Rodent
343 Surgical Prep/Rodent/Recovery Surgery

REQUIREMENTS/COMMENTS
Please ensure that individual(s) performing procedures on live animals, as described in this protocol, are familiar with the contents of this document.

c.c. Approved Protocol   P. Foster, B. Dunn, W. Lagerwerf
Approval Letter   - B. Dunn, W. Lagerwerf

University Council on Animal Care • The University of Western Ontario
Animal Use Subcommittee • Health Sciences Centre • London, Ontario • N6A 5C1 • Canada

Wes⬛rn

Date: May 17, 2006

Dear Dr. **Foster**

A **MODIFICATION** to your "Animal Use Protocol" entitled:

Evaluation of Iron Labeled Melanoma Cells into the Mouse Lymph Node using MRI has been approved.

The protocol **2006-013-03** and yearly expiry date of **March 2007** remain unchanged.

APPROVED CHANGES INCLUDE

☐　　　1.　　**Name change**

☒　　　2.　　**Animal use change(s)**　*Maximum Pain Level:* D

Species	Strain	Other Detail	Housing/Use Location	Number Requested
Mouse	C57Bl/6	14-30g; M/F	HSACF & RRI 2-25 & LHSC-UH MRI suite	132

☒　　　3.　　**Procedural**
　　　　　　Changes to agent use, experimental groups and euthanasia endpoints.

☒　　　4.　　**Other**
　　　　　　Pain class changed from C to D

☐　　　5.　　**Comments**

c.c.　　Approved Modification　　- P. Foster, B. Dunn, W. Lagerwerf
　　　　Approval Letter　　　　　　- B. Dunn, W. Lagerwerf

University Council on Animal Care • The University of Western Ontario
Animal Use Subcommittee • Health Sciences Centre • London, Ontario • N6A 5C1 • Canada

107

Western

03.19.07

This is the 2nd Renewal of this protocol

*A Full Protocol submission will be required in 2010

Dear Dr. Foster:

Your Animal Use Protocol form entitled:

Evaluation of Iron Labeled Melanoma Cells Injected into the Mouse Lymph Node Using MRI – Pilot

has been approved by the Animal Use Subcommittee.
This approval is valid from **04.01.07 to 03.31.08**
The protocol number for this project remains as **2006-013-03**

1. This number must be indicated when ordering animals for this project.
2. Animals for other projects may not be ordered under this number.
3. If no number appears please contact this office when grant approval is received.
   If the application for funding is not successful and you wish to proceed with the project, request that an internal scientific peer review be performed by the Animal Use Subcommittee office.
4. Purchases of animals other than through this system must be cleared through the ACVS office. Health certificates will be required.

ANIMALS APPROVED FOR 1 YR. - Highest Pain Level: D

Species	Other Detail	Housing/Use Locations	Animal # Total for 1 Year
Mouse	C57bl/6 14-30g M/F	HSACF	132

REQUIREMENTS/COMMENTS
Please ensure that individual(s) performing procedures on live animals, as described in this protocol, are familiar with the contents of this document.

c.c. Approved Protocol ` ✓P. Foster, B. Dunn, W. Lagerwerf
      Approval Letter   - B. Dunn, W. Lagerwerf